Revisiting the Global Patterns of Seasonal Cycle in Sea Surface Salinity

Lisan Yu[1], Frederick M. Bingham[2], Tony Lee[3], Emmanuel P. Dinnat[4], and Severine Fournier[3], Oleg Melnichenko[5], and Wendy Tang[3]

[1] Woods Hole Oceanographic Institution, Woods Hole, MA 02543, USA

[2] Center for Marine Science, University of North Carolina Wilmington, Wilmington, NC 28403, USA

[3] Jet Propulsion Laboratory, California Institute of Technology, Pasadena, CA 91109, USA

[4] NASA Goddard Space Flight Center, Greenbelt, MD 20785, USA; Chapman University, CEESMO, Orange, CA 92866, USA.

[5] International Pacific Research Center, University of Hawaii, Honolulu, HI 96822, USA

Main points

1. Annual harmonic of SSS is the most characteristic feature of the seasonal cycle, accounting for 70–80 % of the total observed variance.
2. Semiannual harmonic of SSS is not negligible, especially in regions that are influenced by monsoon or runoff from major rivers.
3. SSS varies around ±0.05 in the subtropical SSS maximum regions, but exceeds ±0.25 in the tropical SSS minimum regions.

Abstract

Seasonal cycle is the largest source of variability for sea surface salinity (SSS) and has a significant influence on the upper-ocean stratification and water-mass formation. The advent of the Argo profiling floats and L-band passive microwave remote sensing in the past one and half decade has significantly improved the sampling of seasonal variations of SSS over the global ocean. Assessing the seasonality of SSS using these recent measurements is important for understanding its relationships with freshwater forcing and ocean dynamics as well as for identifying potential limitations of the SSS observing system. Here we utilize a suite of SSS products from recent satellite and in-situ platforms to revisit seasonal variations of SSS under different freshwater forcing conditions. The result shows that, although the annual harmonic is the most characteristic feature of the seasonal cycle, the semiannual harmonic is not negligible, especially in regions influenced by monsoon and major rivers. The annual and semiannual harmonics account for 70–80 % and 10–16 % of the total observed variance respectively, which together drive the SSS seasonality. The range of seasonal SSS is approximately ±0.05 practical salinity scale (pss) in the subtropical SSS maximum regions, but greater than ±0.25 pss in the tropical SSS minimum regions. However, the seasonal variations of satellite SSS in the 20-40°N latitude range showed erroneous annual and semiannual phases compared with in situ products, the cause of which needs further examination.

Plain Language Summary

The seasonal cycle is the dominant signal of sea surface salinity (SSS) variability. Although often removed in studies concerning climate variability, the seasonal cycle of SSS is of great interest in its own right because is a fundamental state variable. SSS together with sea surface temperature (SST) determines the buoyancy and density stratification of the global upper ocean. Hence, changes to the salinity seasonal patterns alter the timing, magnitude, and spatial distribution of water-column stratification. These in turn affect the location and rate of water mass formation and deep convection, influencing ocean circulation, marine ecosystem, and biogeochemistry. Previous studies of seasonal SSS were based on observations that were sparely distributed in some parts of the ocean. SSS records with seasonal resolution have become more readily available with the advent of the global Argo array of profiling floats since 2003 and L-band passive microwave remote sensing since 2010. This study analyzed a suite of SSS data records from recent satellite and in situ platforms, aiming to provide characterization of the seasonal range of SSS in both the tropical low-SSS regime associated with the Intertropical Convergence Zone (ITCZ) and the subtropical high-SSS regime under the influence of high evaporation.

1. Introduction

The advent of L-band passive microwave remote sensing in last decade (2010 to present) has allowed for the first time the retrieval of global high-resolution sea surface salinity (SSS) from space (Reul et al. 2014; Vinogradova et al. 2019). These new SSS datasets have opened the modern era of salinity sciences, leading to new insights into the role of salinity in ocean circulation, water mass formation, the water cycle, and climate variability and change (Reul et al. 2020). Like many typical time series, the most characteristic signal of satellite SSS is the seasonal cycle, a pattern that is repetitive from year to year and has variability generally greater than intraseasonal, interannual, and longer-timescale variability (Bingham and Lee, 2017; Dinnat et al., 2019). To facilitate the detection of climate-induced fluctuations that have smaller magnitudes, the seasonal cycle is often removed in studies concerning climate variability. However, the seasonal cycle of SSS is of great interest in its own right. SSS is a fundamental ocean state variable, which together with sea surface temperature (SST), determines the buoyancy and density stratification of the global upper ocean. It has been shown that changes to the salinity seasonal patterns alter the timing, magnitude, and spatial distribution of water-column stratification (Maes & O’Kane 2014; Jensen et al. 2016), which then affects the location and rate of water mass formation (Yu et al. 2018; Piracha et al. 2019), deep convection (Gelderloos et al. 2012; Cherniavskaia et al. 2019), and the production and seasonal cycle of ecosystem dynamics (Greene 2013). Systematic and accurate quantification and characterization of seasonal variations of SSS are highly needed. This is especially necessary for satellite SSS observations because they are new and need to be fully evaluated and understood.

There are generally two approaches to obtain the seasonal cycle of a multi-year time series. One is to average values for the same month for different years over the available period.

The other is to subject the time series to harmonic analysis and estimate the amplitudes and phases of the annual and semiannual cycles. Levitus (1986) and Boyer and Levitus (2002; hereafter BL2002) were among the first works that provided a comprehensive view of the annual cycle of global sea surface salinity (SSS) using the World Ocean Atlas 1998 (WOA98) fields of climatological monthly mean salinity (Boyer & Levitus 1994). In particular, BL2002 computed the annual and semi-annual harmonics from Fourier analysis and showed that most of the world ocean has an annual cycle of SSS less than 0.3 on the practical salinity scale (pss). Areas with an annual cycle larger than 0.3 pss include the tropical Pacific and Atlantic under the Intertropical Convergence Zone (ITCZ) and the South Pacific Convergence Zone (SPCZ), the Northern Indian Ocean that is impacted by the monsoons, and the northern North Atlantic that is subject to Arctic meltwater discharge. They also showed that the amplitude of the second harmonic is greater than 0.3 pss only in limited areas, mostly the outflow regions that are affected directly by major rivers including the Amazon (the western tropical Atlantic), Congo and Niger (the equatorial eastern Atlantic), Mississippi (the northern Gulf of Mexico), and Ganges/Brahmaputra (the Bay of Bengal).

The WOA98 climatology is an objectively analyzed gridded product derived from profile data archived in the World Ocean Database 1998 (WOD98; Boyer et al., 1998). Although the total number of SSS observations in the WOD98, accumulated over a 45-year span, exceeds 1.4 million, the spatial and temporal distribution of SSS measurements is highly inhomogeneous. There is a greater data coverage for the northern hemisphere than the southern hemisphere, and in each hemisphere, a greater amount of data for summer months than the winter months and more observations in the open oceans than in the coastal zones. In spite of these uncertainties, the work of BL2002 laid a solid foundation for further study of SSS seasonal variability that uses improved datasets and with enhanced regional foci. For instance, Rao and Sivakumar (2003) used the North Indian Ocean subset of the WOD98 and examined the dynamical contrast between the SSS seasonal distributions of the Arabian Sea (AS) and Bay of Bengal (BoB). Bingham et al. (2010) produced composite maps of near-surface salinity seasonal cycles in the Pacific by adding a significant number of new profiling-float data in the Pacific that were collected since the work of BL2002, and a large thermosalinograph and bucket salinity database collected by French researchers (Delcroix et al., 2005). They also applied harmonic analysis to individual data instead of monthly-gridded values. Chen et al. (2018) took the advantage of the 11-year (2004–2014) Argo monthly-mean fields (Roemmich & Gilson 2009) and conducted harmonic decomposition to obtain the three-dimensional structure of the global salinity seasonal climatology. Interestingly, the annual and semiannual periodicities can be found from the surface all the way down to the Argo sampling depth of ~ 2000 m. There are also a few applications to recent satellite SSS products (e.g., Reagan et al. 2014; Kohler et al. 2018; Melnichenko et al. 2019; Yu 2020).

Wyrtki (1965) pointed out that the harmonic parameters provide a direct measure for the amplitudes of annual and semiannual cycles and supply information regarding how representative they are of the total variance in the time series. These parameters are more straightforward in capturing the dominant harmonic patterns of seasonal variations than a set of monthly maps produced by the averaging approach. However, this approach is not suitable if the objective is to gain an understanding of the processes responsible for the seasonal variations in the time series. In this regard, one often uses the seasonal cycle produced by the averaging approach to compute the contributions of each physical processes (e.g. surface fluxes, advection, and mixing) to the total budgets of salt (for salinity) or heat (for temperature). Seasonal SSS dynamics based on near-surface budget equations have been addressed by numerous studies: Delcroix et al. (1996) and Alory et al. (2012) for the tropical Pacific, Rao and Sivakumar (2003) and Kohler et al. (2018) for the tropical Indian Ocean, Foltz et al. (2008) and Camara et al. (2015) for the tropical Atlantic, Hasson et al. (2013) and Yu (2015) for the pan-tropical ocean, Johnson et al. (2016) for the subtropical ocean, Dong et al. (2009) and Ren et al. (2017) for the Southern Ocean, Yu (2011), Bingham et al. (2012), Vinogradova and Ponte (2013) for the global ocean, Founier et al. (2016) for the plume at the mouth of the Mississippi River, among many others. Some of the studies listed above included both an annual harmonic analysis and a mixed layer salt budget analysis (e.g. Rao and Sivakumar 2003; Bingham et al. 2012; Vinogradova and Ponte 2013; and Kohler et al. 2018).

This study aims to examine the SSS seasonality using satellite SSS products derived from two L-band missions: the Soil Moisture and Ocean Salinity (SMOS) mission by the European Space Agency (ESA) that has been providing continuous SSS data records since its launch in November 2009 (Kerr et al. 2010; Reul et al. 2020), and the NASA Soil Moisture Active Passive (SMAP) mission that has been operating since January 2015 (Entekhabi et al. 2010; Vinogradova et al. 2019). Retrieving SSS from L-band radiometers operates on the principle that the emissivity from the ocean surface is dependent of the dielectric constant of seawater and is a function of salinity, temperature, sea state, polarization, and incidence angle (Swift and McIntosh 1983; Lagerloef et al. 1995; Yueh et al. 2001). Measuring SSS from space is challenging because of the significant dependence on SST and sea state and surface roughness, especially in regions with low SST where the radiometric sensitivity to SSS is much reduced. The sensitivity decreases from 0.7K per pss change for SST of 30°C to 0.25 K per pss change for SST of 0°C. The accuracy of SSS retrievals are affected not only by geophysical signals (e.g. SST, sea surface state such as roughness, foam, and whitecaps) but also by external perturbing factors including extraterrestrial contributions (e.g. galactic/cosmic background radiation and sun glint), antenna-radiation emissions, Faraday rotation in Earth's ionosphere, atmospheric attenuation, and Radio Frequency Interference (RFI). The latter results from the unauthorized use of the protected L-band or out-of-band contamination in some coastal areas or leakage of other radar signals into L-band (Boutin et al. 2004; Le Vine et al. 2005; Reul et al. 2007; Oliva et al. 2012; Dinnat et al. 2019). SMOS and SMAP SSS products have been validated extensively with in situ salinity measurements, showing that the accuracy of 0.2 pss can be met between 40°S and 40°N (Boutin et al. 2018).

The focus of this study is the ocean between 50°S and 50°N, where the open-water surface temperature is mostly between 5–30°C throughout the year and SSS retrievals are better validated. The study has two objectives. The first is to revisit the WOA98-based seasonal patterns constructed by BL2002 using much higher time and space resolution satellite SSS products. Unlike BL2002 that linked the annual harmonics of SSS to those of evaporation-minus-precipitation (E – P) flux and river runoff for the forcing of SSS seasonal variations, this study focuses only on SSS patterns and the consistency between satellite and in situ products in producing the patterns. We will examine seasonal variability in four commonly used SSS products, two from SMAP (Fore et al. 2020; Meissner et al. 2019) and two from SMOS (Boutin et al. 2019; SMOS-BEC Team, 2019), which are produced independently by different groups using different retrieval algorithms. To provide an in-situ reference, two in situ gridded salinity products are included: the salinity product gridded from Argo profile floats (Roemmich & Gilson 2009; hereafter referred to as the Argo product) and the version 4 of the Met office Hadley

Centre “EN” series of monthly objective analysis of salinity (Good et al. 2013; hereafter referred to as the EN4 product).

The second objective is to expand beyond the focus on the tropical SSS variability in BL2002 to include the characterization of the seasonal cycle of the subtropical SSS. Dominant features in the study domain between 50°S and 50°N are the fresh surface water (the so-called SSS minimum or simply Smin) in the tropics and the salty surface water (the so-called SSS maximum or Smax) in the northern and southern subtropics (Gordon et al., 2015), both of which mirror closely the maxima and minima in the global E–P patterns (Schanze et al., 2010; Schmitt 2008; Yu et al. 2020). Satellites provide unprecedented data coverage over the entire globe with revisit every 2–3 days for SMOS and SMAP. Therefore, an update of BL2002 is deemed necessary to better characterize the seasonality of Smin and Smax.

The paper is organized as follows. A description of the satellite and in-situ SSS datasets and the method is provided in Section 2. Mean and seasonal variability of SSS are evaluated in Section 3. The results obtained from the harmonic analysis are presented in Section 4. Characterization of Smin and Smax is given in Section 5. Summary and discussion are given in Section 6.

2. Data and methods

2.1 Data sets

The major characteristics of the SSS products we will use in this study are listed in Table 1. A brief description of each dataset is provided below.

The two SMAP products are the SMAP Level 3 version 4.3 by Jet Propulsion Laboratory (JPL) (hereafter referred to as SMAP JPL) (Fore et al. 2020), and the SMAP Level 3 Remote

Sensing Systems (RSS) product (hereafter referred to as SMAP RSS) recently released version 4.0 (Meissner et al. 2019). SMAP JPL features a 60-km spatial resolution and 8-day running mean dataset and also a monthly average dataset, both distributed on 0.25°×0.25° grids (For et al. 2020). SMAP RSS is resampled onto 0.25°×0.25° from a 70-km spatial resolution using a Backus-Gilbert type optimum interpolation (OI) in order to reduce random noise and mapped to monthly and 8-day running means (Meissner et al., 2018). The SMAP products are available from April 2015 to the present and distributed by the NASA PO.DAAC. Monthly-mean datasets were used in this study.

The two SMOS products are the SMOS SSS Level 3 maps produced by Laboratoire d'Océanographie et du Climat (LOCEAN) and Centre Aval de Traitement des Données SMOS (CATDS) (Boutin et al. 2019; hereafter referred to as SMOS LOCEAN), and the Level 3 version 2 SMOS SSS global product from the Barcelona Expert Center (BEC) (SMOS-BEC Team, 2019; hereafter referred to as SMOS BEC). SMOS LOCEAN has applied systematic bias correction using an improved de-biasing technique, which improves ice filtering and SSS at high latitudes (Boutin et al. 2019). The 9-day running mean maps have 25-km x 25-km spatial resolution and available from January 2010 onward. SMOS BEC data are generated using a debiased non-Bayesian approach (Olmedo et al. 2017) that corrects the systematic biases caused by the presence of land masses and radio interference, and improves the data gaps due to the non-convergence of the retrieval algorithm. The 9-day running objective analyzed L3 maps are provided daily at 0.25°× 0.25° spatial resolution and available from January 2011 to December 2019.

The two in situ gridded SSS products are the Argo (Roemmich and Gilson 2009) and EN4 (Good et al. 2013) monthly objective analyses. The Argo product is constructed from more than 3000 autonomous profiling floats over the global ocean. It is obtained by first estimating the time-mean field using a weighted local regression fit to several years of Argo data and then performing optimal interpolation on the mean-subtracted monthly residuals to obtain the interpolated anomaly fields on 1°×1° grids. The salinity data of the topmost layer at the depth of 2.5 m is used as SSS in the analysis. The EN4 1°×1° gridded monthly data products are compiled from quality controlled temperature and salinity profiles that are sourced from the Global Temperature and Salinity Profile Programme (GTSPP), World Ocean Database 2009 (WOD09), and Argo. The use of non-Argo data is essential in regions where Argo floats are limited or not available, such as in shallow coastal waters, marginal seas, and sea-ice marginal zones. The topmost grid level of EN4 is at the depth of 5.25 m below the surface, and is used for comparison with satellite SSS products.

It should be noted that the Argo and EN4 SSS are considered to be a bulk SSS, representative of the salinity at about 5-m depth. Satellite SSS is a skin SSS, determined by the depth at which the incoming power density is reduced by two orders of magnitude. For L-band microwave radiometers, the skin layer is about 1 cm at SST of 20°C (Swift 1980). Skin SSS can be different from bulk SSS if there are vertical salinity gradients between the two measurement depths (Yu 2010; Boutin et al.2016; Drucker and Riser, 2014; Henocq et al., 2010). Knowledge of the skin-bulk SSS differences over the global ocean is limited and hence, a degree of caution should be exercised in interpolating the findings of this study. Another major difference between satellite SSS and in situ data is the sampling frequency, both in space and time. How will this affect their capability in resolving the seasonal cycle at annual and semi-annual scale

The in situ gridded products from Argo and EN4 are available on a monthly basis. To be consistent, monthly-mean fields were used for all four satellite products. All six products are available for the three full years, 2016-2018, and so these three years are used as the base period in this study. The focal domain is the ocean basin between 50°S and 50°N where SST is sufficient high and SSS products are better validated. For Harmonic analysis of satellite SSS at higher latitudes (50°N/S poleward), readers are referred to recent studies by Kohler et al. (2018), Garcia-Eidell et al. (2017 & 2019), Fournier et al. (2019), Tang et al. (2018 & 2019), and Yu (2020).

2.2 Harmonic analysis

A least-squares fitting of the annual and semi-annual harmonics to the time series at each grid is performed based on the following equation (Wyrtki 1965; Wilks 1995):

$$S(t) = S_0 + A_1 \cos(\omega_1 t + \varphi_1) + A_2 \cos(\omega_2 t + \varphi_2) \quad (1)$$

where S is the monthly-mean SSS at time t expressed in months, S_0 is the mean annual salinity, ω_1 and ω_2 are the annual and semiannual frequencies expressed as $\omega_1 = 2\pi/12$ months, $\omega_2 = 2\pi/6$ months, and A_1, A_2, φ_1, and φ_2 are the amplitudes and phases of the annual and semiannual harmonics, respectively. At each grid, the amplitudes (A_1 and A_2) and phases (φ_1 and φ_2) are computed from the regression procedure using the three-year time series.

3. Mean and seasonal variability of SSS

3.1 Time-mean SSS fields

The three-year (2016–2018) mean SSS fields constructed from the six products are shown (Figure 1). Fundamental features of the mean SSS distribution include the contrast between the saltier Atlantic Ocean and the fresher Pacific and Indian Oceans at all latitudes, the fresher tropical ocean in the precipitation zones associated with the ITCZ and SPCZ, and the saltier subtropical ocean associated with the highly evaporative zones under the subtropical highs. A well-defined Smax center exists in all subtropical regimes of the Pacific, Atlantic, and the Indian Oceans.

The tropical Smin and the subtropical Smax reflect the time-mean interactions between the E–P flux, ocean circulation, and mixing processes (e.g. Dessier and Donguy 1993; Delcroix et al. 1996; Donguy and Meyers 1996; Talley 2002; Gordon et al. 2015). Marked low-salinity surface waters are also noted in the coastal areas near major rivers, including the northern Bay of Bengal, the eastern equatorial Pacific and Atlantic, the western equatorial Atlantic, the East China Sea, and the northwestern Atlantic shelf region. This localized freshening is dictated by hydrological forcing through local rainfall and river discharges (Gierach et al. 2013; Grodsky et al. 2014; Chao et al. 2015; Fournier et al. 2017a&b; da Silva & Castelao 2018). In general, the plume features are underestimated in in situ products.

3.2 Ensemble average

The ensemble average of the six mean products and the standard deviation (STD) between them are shown (Figures 2a-b). The STD field is used as a measure of the spread in magnitude between the products. The six mean patterns agree well in the open ocean away from the coast and equatorial regions, with STD less than 0.05 pss. Considerable differences, with STD greater than 0.2 pss, appear in the periphery of the coast areas, the marginal seas, the ITCZ and SPCZ regions, and some regions in the higher latitude bands of 40°N/S poleward.

To facilitate the characterization of seasonal variability associated with the tropical Smin and the subtropical Smax, nine areas surrounding the Smin and Smax centers (denoted by nine boxes in Figure 2a) are selected for detailed analysis in the following sections. Locations, abbreviated names, the product ensemble SSS mean and STD (spread) within the nine boxes are listed in Table 2. There are three Smin boxes (1-3) in the tropical low-SSS regime, one in each basin. These boxes are located primarily in the open waters away from the direct influence of main rivers. In addition, six subtropical Smax boxes (4-9) are selected around the subtropical high-SSS zones in both the Northern and Southern Hemispheres. The ensemble mean SSS averaged over each box and the enclosed isohaline of SSS equal to the box-averaged SSS value are shown.

The STD, or the spread between product, differs with the box (Table 2), being generally larger in the tropical Smin regime and smaller in the subtropical Smax regime. STD exceeds 0.05 pss in two Smin boxes, the eastern tropical Pacific (Box 1) and the Bay of Bengal (Box 3), and one Smax box in the Arabian Sea (Box 6). STD in the other six boxes ranges between 0.02 – 0.04, showing that the mean patterns of the products have a good agreement in these boxed areas.

3.3 Mean differences from Argo

The Argo mean field is taken as a reference to assess how each mean pattern deviates from the Argo reference base. The mean fields of the other five products were averaged into the Argo 1°× 1° grids and the Argo mean field was subtracted from each product (Figure 3). The pattern of the difference anomalies between satellite and Argo varies with product.

SMAP JPL (Figure 3a) is saltier than Argo (positive anomalies) in the equatorial and northern basins but fresher (negative anomalies) in the most of the Southern Hemisphere. This north-south contrast in the sign of SSS difference anomalies is particularly pronounced in the Indian and Pacific Oceans. Large positive anomalies (>0.2 pss) are found in three bands in the

North Pacific: the equatorial Pacific, a zonally-oriented band north of 40°N, and the peripheral areas of the west coast of North and South America. Large positive anomalies also present at high latitude Southern Indian and Atlantic oceans (40°S poleward). SMAP RSS (Figure 3b) are generally fresher than Argo over open ocean, with marked negative anomalies (< –0.2 pss) in the Arabian Sea, the high-latitude Southern Ocean (40°S poleward), and the west and north Pacific ~40°N. Large positive anomalies (> 0.2 pss) are present in the coastal regions adjacent to the South American continent and the neighborhood of the Caribbean Seas and Gulf of Mexico.

SMOS LOCEAN (Figure 3c) has also a north-south contrast in the sign of its difference anomalies relative to Argo, with magnitude generally less than 0.1 pss. Major positive anomalies (> 0.2 pss) are in the Arabia Sea, the western tropical Pacific, and the northern North Atlantic (40°N poleward). SMOS BEC (Figure 3d) shows a band of large positive anomalies (>0.2 pss) in the tropical Pacific and eastern Indian Ocean between 10°S and 20°N, where the Smin waters are featured in responding to the freshwater input from the ITCZ and SPCZ. Aside from this tropical zone, SMOS BEC is fresher than Argo, particularly in the North and South Atlantic Ocean.

The two *in situ* gridded products, EN4 and Argo, have a good agreement (Figure 3f), and the differences between them are generally less than 0.1 pss except for a few locations such as the western boundary currents (e.g. the Gulf Stream off of North America and the Kuroshio Extension off Japan) and in coastal regions under influence of major river discharge. These localized discrepancies are mostly caused by two factors: the lack of Argo float observations in coastal regions and the use of WOD09 as background information to fill in data gaps in EN4.

3.4 Seasonal variability of SSS

The STD of the monthly-mean SSS values is used as a measure of SSS seasonal variability (Figure 4). Argo shows that the seasonal STD is dominated by large STDs (>0.4 pss) in the following areas: the pan-tropical low salinity zone under the ITCZ and SPCZ, the near coastal areas affected by the Amazon plume in the western tropical Atlantic (Grodsky et al. 2014; Fournier et al. 2017b) and by the Congo and Niger rivers in the eastern equatorial Atlantic (Reul et al. 2014; Chao et al. 2015), the northwestern Atlantic shelf region particularly south of the St. George's and Newfoundland banks (Grodsky et al. 2017), the northern Gulf of Mexico bordering the Mississippi (da Silva and Castelao, 2018), the vicinity of the western South Atlantic near 35°S, 55°W under the influence of the Plata river (Piola et al. 2005), the Bay of Bengal impacted by monsoon and the Ganges/Brahmaputra river (Momin et al. 2015; Fournier et al.2017a), and the southeastern Arabian Sea centered at 8°N, 75°E, known as the Laccadive Sea region (also called the Lakshadweep Sea) (Bruce et al. 1994; Schott and McCreary 2001). All of these high STD regions are in direct response to the freshwater sources from rainfall and/or river discharge, except for the high STD in the Laccadive Sea of the Arabian Sea. In the latter, the source of the pronounced seasonal variability of SSS is the incursion of the water from the Bay of Bengal during November to February (Shenoi et al., 1999). During that period, the Northeast Monsoon generates East Indian Coastal Current (EICC) that flows equatorward along the Indian and Sri Lanka coast and brings low-salinity water from the Bay of Bengal to the southeast Arabian Sea (D'Addezio et al., 2015), causing a sea-surface freshening by more than 1 pss compared to October (Rao and Sikakumar 2003).

The STD patterns show that SMOS BEC product is significantly different from other products. The three satellite products, SMAP JPL, SMAP RSS, and SMOS LOCEAN (Figures 4a-d) have a broad agreement with Argo in the tropical regions but differ from Argo in two other areas. One is the North Pacific north of 40°N where abnormally high STDs (>0.4 pss) are shown in SMAP JPL, SMAP RSS, and SMOS LOCEAN. The other area is the western Arabian Sea off the coast of Oman where high STDs (>0.4pss) are present in the two SMOS products, but not in the SMAP products nor in the in situ products. Zonal bands of high STDs are also seen in SMAP JPL at high southern latitudes (poleward of 40°S). Among the four satellite products, SMOS BEC has the weakest STDs, particularly in the tropical Pacific under the ITCZ and SPCZ.

The EN4 STD pattern is similar to that of Argo over the open ocean, but has enhanced STD values in the marginal seas and coastal areas. The differences are due primarily to the differences in data coverage. Argo floats do not sample shallow seas and coastal areas, whereas the EN4 product includes in situ measurements from all available platforms and refers to long-term climatology as background information in the presence of data gaps (Good et al. 2003).

One marked difference between satellite and in situ SSS products is the mean level of STD in the open ocean away from the tropical rain bands and the coastal zones. In these seasonally quiescent regions, the STDs in Argo and EN4 are weak, at 0.1 pss or less. Satellite products have considerably higher STDs, with magnitude generally above 0.1 pss. The differences suggest that satellite products may contain a higher level of random noise, or that the in situ products underestimate seasonal variability in the open ocean.

4. Patterns of Harmonic Modes

4.1 Annual harmonic of SSS

Amplitudes of the estimated first harmonic (A_1 in Eq. (1)) in the six SSS products (Figure 5) show that the regions of large STDs (>0.3 pss; Figure 4) are also regions of pronounced annual cycle, with SSS amplitudes exceeding 0.3 pss. As discussed in the previous section, these areas are predominantly influenced by the freshwater sourced from either rainfall or river discharge, demonstrating the intimate connection of regional SSS to the ocean and terrestrial water cycle. The six products agree well with each other on the pattern of annual amplitude and also compare well with the WOA98-based pattern estimated by BL2002. It is worth noting, however, that SMOS BEC has the weakest annual amplitude over the global ocean among all satellite products, with almost no annual variation in the extratropical open ocean. SMAP JPL has spuriously large annual amplitudes in the sub-polar North Pacific, poleward of 40^{o}N, and in the Southern Ocean.

Differences from BL2002 are most noticeable in two aspects. The first is that the present maps have a larger range of amplitude and sharper SSS fronts in regions of strong annual amplitude (>0.3 pss). The finer spatial and temporal scales that satellites are capable of resolving allow satellite products to better represent the narrow bands of large SSS amplitudes associated with SSS fronts in both the open ocean and coastal and marginal seas. The latter include the Indo-Pacific throughflow area and the surrounding seas of Indonesia, the western Pacific marginal seas consisting of the South China Sea, the East China Sea, and the Sea of Japan. The representation of the three narrow zonal bands of SSS annual amplitude that are associated with the ITCZ, the equatorial cold tongue, and the Costa Rica dome (Alory et al.2012) in the far eastern Pacific fresh pool (100–80°W, 0–10°N) is a striking example of the advantages of satellite SSS remote sensing. Neither Argo nor EN4 are able to fully represent the fine spatial distinctions associated with these three narrow zonal bands. The second aspect is that the present maps of SSS annual amplitude have substantially large amplitude (~0.3 pss) in the subtropical Smax regions, in contrast to the results of BL2002 where annual amplitude outside of the tropical regions is weak and in isolated areas. The improved representation of Smax by satellite observations provides an incentive for an improved characterization of Smax and its seasonal variability.

The phase of the estimated annual cycle (φ_1 in Eq. (1)) represents the time (month of the year) at which the maximum value of the SSS annual cycle (i.e, the saltiest surface water) occurs. Patterns of the annual phase (Figure 6) suggest that the six products are consistent in describing the progression of the maximum amplitude of the SSS annual cycle in the tropical ocean. For instance, the SSS at the 10°N latitude band in the tropical Pacific reaches the annual maximum in April-May when the ITCZ is located near the equator, whereas SSS near the equator has the annual maximum in July-August where the ITCZ moves farthest north near 10°N. Similar annual phase progression is also shown in the tropical Atlantic and Indian Oceans, with a noted exception of SMOS BEC which has a phase shift in the North Indian Ocean.

Outside of the tropical oceans, satellite products deviate among one another in two zonal bands. One is in the southern hemisphere between 50–20°S, where SMOS BEC is markedly different from the other products, showing that the annual high SSS values occur predominantly in February. The second location is in the northern hemisphere between 20–40°N centered in the northwestern Pacific off the coast of Japan (120°E – 180) and the northwestern Atlantic off the coast of the United State and Canada. In these regions, the phase in SMOS BEC and SMOS LOCEAN is shifted by about 6 months. The SMAP products, particularly SMAP JPL, are similarly out of phase with the in situ products, though to a lesser degree. SMAP JPL has a phase shift of about 3 months in the northwestern Pacific. Apparently, satellite products have seasonal biases in this zonal band in terms of phase. One possible factor contributing to such seasonal biases is the effect of RFI. The percentages of SMAP land samples suspected to be influenced by RFI are highly concentrated in the regions such as Japan and northeastern China as well as

Europe (e.g., Piepmeier et al 2014). Even if some SMAP measurements over the ocean that are obviously affected by RFI are excluded, low-level RFI can still affect satellite SSS retrievals. SMOS is also significantly affected by RFI and land contamination in these regions, and exhibits very large positive biases in radiometric observations (resulting in fresh biases in retrieved salinity) extending to 160°E and beyond east of Japan (Martín-Neira et al., 2016). Some mitigation and corrections schemes employed in the SSS products to reduce the impact of RFI might introduce other errors. Other contributors for the seasonal biases in satellite SSS are also possible. Effort is needed to spin down the causes.

4.2 Semiannual harmonic of SSS

Amplitudes of the estimated second harmonic (A_2 in Eq.(1)) in the six products are shown in Figure 7. Argo and EN4 indicate that the semiannual component is small, far less than 0.1 pss, over most of the global ocean. Areas with significant semiannual component (amplitude > 0.3 pss) are the near coastal regions bordering to large rivers, including the Amazon (the western tropical Atlantic), Congo and Niger (the equatorial eastern Atlantic), Mississippi (the northern Gulf of Mexico), Ganges-Brahmaputra (the Bay of Bengal), Yangtze River (the South China Sea), and Rio de la Plata estuary (at ~35°S on the Atlantic coast of South America). This depiction is consistent with BL2002. Areas with significant semiannual component that are shown in present satellite maps but absent in BL2002 include the marginal East China Sea and the Sea of Japan where the semiannual cycle has amplitude of 0.3 pss, and the eastern equatorial Pacific where the semiannual amplitude is of order 0.2 pss along a few narrow zonal bands. Satellite products are generally in good agreement with Argo and EN4 except for coastal regions mainly in the North Pacific. In addition, SMAP JPL has a stronger semiannual amplitude between 50–40°S. SMOS LOCEAN displays a zonal band of semiannual amplitude of 0.3 pss near 40°N, possibly related to the effect of RFI.

Phases of the estimated semiannual cycles (φ_2 in Eq. (1)) (Figure 8) show that all products agree well in the tropical ocean. Outside of the tropics, SMAP JPL and RSS have an overall in-phase relationship with Argo and EN4, whereas SMOS LOCEAN and BEC are generally out of phase with both in situ and SMAP product, particularly in the northern latitudes between 20–50°N.

4.3 Variances

The annual and semiannual cycles of SSS at each grid location were constructed using the estimated amplitudes and phases of the respective first and second harmonics, and the two modes were then combined to reconstruct the seasonal variations. Variances of the first harmonic, second harmonic and the sum were computed. The ratio of each of these relative to the total variance represents the percentage of the total variance that can be accounted for by the given mode. Spatial patterns of the percentage of total variance accounted by the annual and reconstructed seasonal cycles are shown in Figures 9 and 10, respectively. Basin averages of the percentage contributions from all the three components (i.e. the annual, semiannual, and the reconstructed seasonal cycles) were also made for the three individual basins (Pacific, Atlantic, and Indian) and the global ocean between 50°S – 50°N and summarized in Table 3.

The spatial pattern of the annual harmonic contribution to the total SSS variance (Figure 9) indicates that, in general, the percentage of total variance that can be explained by annual harmonic is proportional to the annual amplitude. The areas where annual harmonic has a large contribution (>80%) to the total variance are often the areas where annual amplitudes are greater than 0.2 pss (Figure 5). One exception is the higher southern latitudes (south of 25°S) where annual amplitudes in most areas are substantially lower than 0.1 pss. For satellite products, the weak annual harmonic in the region corresponds to a low contribution to the total variance (<20%), whereas for in situ products, the weak annual harmonic in the region can still account for a substantial percentage of the total variance. This difference may reflect the impact of noise in the data on the computation of the percentage contribution. As shown in Figure 4, the total variance in in situ products is much weaker than in the satellite products in the extratropical regions away from marginal seas and the western boundary currents. The weaker total variances boost the percentage contribution of the in situ products even if their annual variances are as weak as those in satellite products.

The percentage contribution is increased by 10-20% almost everywhere over the globe when the semiannual harmonic is combined with the annual harmonic to obtain the reconstructed seasonal cycle (Figure 10). Two harmonic modes can account for most of the total variance in EN4 and Argo, but much less so for the variances of the four satellite products. The differences between products can be better assessed using the basin averages listed in Table 3. Four features are noted. First, EN4 shows that, globally, 95% of the total SSS variance can be explained by the first two harmonic modes, with 84% of the variance coming from the annual harmonic and 11% from the semiannual harmonic. The partition of annual and semiannual contributions is similar in the Pacific and Atlantic Oceans, but is titled slightly toward the semiannual mode in the Indian Ocean due to the influence of monsoon forcing. Second, the first two harmonic modes in Argo contribute to about 87% of its total SSS variance, which is about 8% less than those in EN4, and the main cause is the lower contribution of the annual harmonic in Argo. Third, SMAP RSS and SMOS LOCEAN show that the annual and semiannual harmonics have similar percentage contributions to Argo in all basins except for the Pacific where harmonic analysis is affected by the impact of RFI. Lastly, SMAP JPL and SMOS BEC show substantially lower percentage contributions from the two harmonic modes in both Pacific and Atlantic, but are comparable to other products in the Indian Ocean.

5. Characterization of the Smin and Smax

5.1 The tropical Smin (Boxes 1–3)

Boxes 1 (Smin-Pac), 2 (Smin-Atl), and 3 (Smin-BoB) represent the Smin in the open waters of the tropical Pacific, Atlantic, and Bay of Bengal, respectively (Figure 2a). The annual, semiannual, and the reconstructed seasonal cycles averaged over the three boxes (Figure 11) reveal that all products, except for SMOS BEC, have a remarkable agreement in Box 1 (Smin-Pac) and Box 2 (Smin-Atl). Seasonal variations of the SSS in Boxes 1-2 are dominated by the annual cycle, higher in March-April and lower in September-November in accordance to the seasonal migration of the ITCZ (e.g. Delcroix 1998; Bingham et al. 2010; Guimbard et al. 2017; Melnichenko et al. 2019).

For Box 3 (Smin-BoB), the annual cycles of the satellite products have a two-month phase lead compared to that in situ products, though all products agree well on the semiannual cycle. The areas covered by Box 3 are subject to massive runoff from major and minor rivers, including the Godavari in the west, the Ganges/Brahmaputra in the north, and the Irrawaddy in the east. The amplitude of the semiannual cycle of SSS is nearly equal to the annual cycle of SSS, and hence, most of reconstructed seasonal cycle shows a mixed annual/semiannual oscillation, with maximum in June and minimum in October. It is noted that the spread between products is relatively large, especially in the months of January-May and October.

The seasonal SSS minimum in Box 3 (Smin-BoB) occurs in October after the end of the southwest monsoon, and the timing possibly reflects the cumulative effects of the freshwater input through local rainfall and river discharge (BL2002; Rao & Sivakumar 2003). By comparison, the seasonal SSS maximum in June is induced by the influx of high salinity water from the Arabian Sea associated with the eastward Summer Monsoon current (SMC) (Jensen 2001). This saltier water, however, is denser and slides under the lighter surface water of the Bay (Sasamal 1990). Vinayachandran et al. (2013) suggested that eddy-driven vertical mixing constitutes the main mechanism for pumping the saltier, subsurface water into the surface layer along the meandering path of the SMC, which enables the bay to stay salty despite a large net freshwater input.

5.2 The subtropical Smax in the Northern Hemisphere (Boxes 4–6)

Three Smax boxes in the Northern Hemisphere are Boxes 4 (Smax-NPac), 5 (Smax-NAtl), and 6 (Smax-AS) (Figures 2a and 12). SMOS BEC and LOCEAN have very small combined amplitudes in these three boxes. In contrast to the other products, there is substantial mismatch, a few months, in phase in boxes 4 and 5 between SMOS and in situ products for both annual and semiannual harmonics. SMAP JPL and RSS are mostly in phase with the in situ products, although SMAP JPL has a stronger amplitude and SMAP RSS has a weaker amplitude compared to in situ products, particularly in Boxes 4-5.

Amplitudes of the annual and semiannual harmonics are both weak in Boxes 4-5 for all products. The Argo product has annual and semiannual amplitudes of about 0.04 and 0.01 pss, respectively, in Box 4, and about 0.06 and 0.02 pss, respectively, in Box 5 (Table 4). The reconstructed seasonal cycle in Box 4 is also weak, with lower SSS in March-May and higher

SSS in September-December and no clear peak timings. The Argo combined seasonal cycle in Box 5 is better defined, showing a seasonal minimum in April and a maximum in September. The SSS peak timing differs between Boxes 4 and 5. EN4 agrees with Argo in Box 5 but is slightly weaker in Box 4. Satellite products deviate considerably in Box 4. This is also a region where seasonal variations of SSS in both satellite and in situ data are very weak.

For Box 6, the SMAP and in situ products suggest that the reconstructed seasonal cycle has a strong seasonal minimum (~0.28 pss) in March-April but a prolonged high SSS seasonal maximum (~0.15 pss) from August to December. The asymmetry of the seasonal cycle is caused by the superposition of the semiannual cycle and annual cycles. The annual minimum during January – June is enhanced because it is coherent with the phase of the semiannual cycle, while the annual maximum is weakened and lengthened during July – December because it is opposite to the phase of the semiannual cycle. Box 6 covers the open area of the Arabian Sea, where the SSS variability is influenced not only by local evaporation and rainfall but also by freshwater transport out of the BoB by the westward North Monsoon Current during the winter monsoon from November to February (Shenoi et al., 1999; Jensen 2001; Rao & Sivakuman 2003). The latter causes a sea-surface freshening by more than 1 pss compared to October in the southeastern Arabian Sea, known as the Laccadive Sea region (Bruce et al. 1994; Schott & McCreary 2001; Rao and Sikakumar 2003).

5.3 The subtropical Smax in the Southern Hemisphere (Boxes 7–9)

The three Smax boxes in the Southern Hemisphere are Boxes 7 (Smax-SPac), 8 (Smax-SAtl), and 9 (Smax-SInd) (Figures 2a and 13). The annual cycle peak timings in these three boxes are similar, all showing higher SSS in April-May and lower SSS in September-October.

In general, the annual amplitude is around 0.05 pss in Boxes 7&9 and slightly larger in Box 8, at about 0.1 pss. SMOS BEC, though, differs from this timing in all these boxes.

The semiannual component is more pronounced in satellite products than in in situ products, and imposes substantial modulation on the annual cycle, particularly in Box 9. This is different from Argo and EN4. The Indian Ocean monsoon climate is limited mostly to the regions north of 15°S (Schott & McCreary 2001), so the area in Box 9 located at latitudes between 35 – 25°S is not under the direct influence of the monsoon. Hence, the presence of a strong semiannual cycle in satellite-derived SSS products is either not correct, or related to some influence other than the monsoon.

5.4 Smax in the areas bounded by fixed boxes and by fixed isohalines

Amplitudes of annual and semiannual harmonics averaged over the Smax boxes (Table 4) reveal an interesting result: if Box 6 (Smax-AS) is excluded to avoid the region influenced directly by monsoon, the annual amplitudes in the Smax boxes are mostly around 0.05 pss except for Box 8 (Smax-SAtl) that has a slightly higher amplitude about 0.1 pss. Since the semiannual component is weak in these five Smax boxes, the seasonal range (i.e., maximum minus minimum) of the reconstructed seasonal cycle is about the same as the annual cycle (Table 5).

One question is raised as to how much the seasonal range in a selected Smax box represents the seasonal range of the Smax bounded by a reference isohaline. The key difference between the two approaches is that the control area enclosed by a reference isohaline bounds the feature of interest throughout the calendar year and changes with time (Bryan & Bachman 2015; Gordon et al. 2015; Melzer & Subrahmanyam 2015; Yu et al. 2018; Hasson et al. 2013b), while a fixed box does not change with time and hence, does not conserve the feature. To assess the impact of the approach on the quantification of the Smax seasonality, the seasonal cycles of Smax enclosed by a reference isohaline were constructed in the vicinity of the five Smax boxes over the subtropical oceans (i.e., Boxes 4, 5, 7, 8, & 9). To do so, the full seasonal cycle was first constructed from Eq. (1) using the first two harmonics. The reference isohaline that equals the SSS value averaged over the corresponding box was then selected (Figure 2a). The SSS values bounded by the reference isohaline were averaged for each calendar month, yielding a seasonal cycle of Smax for a control area. The seasonal cycles thus obtained were demeaned and compared to the corresponding box-averaged seasonal cycles constructed from the first two harmonics.

Figure 14 shows the ensemble averages of the two types of the Smax seasonal cycle at the five Smax regions, with the lighter color shadings denoting one standard deviation of the spread of the six datasets. Interestingly, the seasonal range of the box-averaged Smax is only slightly larger than the isohaline-bounded Smax at all locations except for the Smax in the subtropical South Atlantic. In the latter, the amplitude of the box-averaged Smax is around 0.1 pss, about twice as large as the amplitude of the isohaline-bounded Smax. The discrepancy indicates that the location change of the Smax core in this region is small and Box 8 (Smax-SAtl) may be affected by lower SSS values that fluctuating in and out of the box with season. Hence, the isohaline-bounded approach appears to be a more accurate way for quantifying the seasonal range of the Smax. If doing so, the seasonal range of the Smax core in all five subtropical regions does not exceed 0.05 pss, with the Smax in the Southern Indian Ocean being the weakest and the Smax in the South Atlantic being the largest.

The ensemble seasonal cycles of the isohaline-bounded Smax (Figure 14) are in good agreement with those isohaline-bounded Smax cycles reported by Gordon et al. (2015; Figure 3) that used the Monthly Isopycnal/ Mixed Layer Ocean Climatology (MIMOC; Schmidtko et al., 2013) compiled from Argo, TSG, and conductivity-temperature- depth (CTD) data. There is one exception, though, for the Smax in the North Pacific where the ensemble pattern here is obviously erroneous. The cause of the deviation is yet to be examined. The satellite products, SMAP RSS, SMOS LOCEAN, and SMOS BEC, all have low or negative correlations with the seasonal cycle based on Argo (Table 5). The spurious seasonal cycle is also seen in the two SMOS products in the subtropical North Atlantic (see the correlation coefficients for Box 5 (Smax-NAtl) in Table 5).

6. Summary and discussion

SSS records with sufficient seasonal resolution over much of the global ocean have become available only in the past one and half decades thanks to the advent of the Argo profiling floats and L-band passive microwave remote sensing. This study utilized six SSS data products from satellite and in situ platforms to assess the SSS seasonality in the global ocean between 50°S – 50°N. Three objectives are addressed: to revisit the dominant harmonic patterns of SSS that were first produced from the World Ocean Atlas 1998 by BL2002, to expand the analysis into the seasonal characterization of both the tropical salinity minimum zones and the subtropical salinity maximum centers, and to assess the fidelity of satellite SSS in presenting the seasonal cycle of SSS form the open ocean to the coastal regions. For the latter, nine boxes were selected in the vicinity of the Smin and Smax over the global basin. The major results of the study are summarized as follows.

The annual harmonic is the most characteristic feature of the seasonal cycle, but the semiannual harmonic is not negligible, particularly in the Northern Indian Ocean under the influence of monsoonal circulation and the near coastal regions bordering to large rivers, including the Amazon (the western tropical Atlantic), Congo and Niger (the equatorial eastern Atlantic), Mississippi (the northern Gulf of Mexico), and Ganges-Brahmaputra (the Bay of Bengal). When the two harmonics are combined to reconstruct the seasonal cycle, the semiannual harmonic shows a modulation effect on the annual harmonic. In the Bay of Bengal and the Arabian Sea, the semiannual amplitude is large enough to amplify the annual cycle if the two harmonics have the same phase, and weakens or lengthens the annual cycle if the two have opposite phase.

The annual and semiannual harmonics account for 70–80 % and 10–16 % of the variance of the observed seasonal variations globally (50^{o}S-50^{o}N), which together drive the SSS variations. Satellite SSS products are primarily consistent with in situ products on the amplitudes and phases of the two harmonics. However, the study also found that satellite SSS retrievals in the Northern Hemisphere (20-40°N) have erroneous annual and semiannual phases compared with in situ products. Whether it is caused by RFI or other factors need to be investigated.

The amplitude and seasonal range of the seasonal cycle of SSS averaged over each of the nine boxes is summarized in Figure 15. For the boxes located in the open ocean away from monsoon-influenced regions, the seasonal range of SSS is mostly ±0.05 pss in the subtropical Smax regime, and ±0.25–0.40 pss in the tropical Smin regime. Obviously, the seasonal amplitude of SSS is larger in the precipitation-dominated tropics and considerably weaker in the evaporation-dominated subtropics. The differences in amplitude between the Smin and Smax regimes underline the different effects of evaporation and precipitation on the stability of the water column (Yu 2010). Evaporation increases SSS. If the SST change is not considered, this causes an increase of surface density, leading to a destabilization of the upper-ocean stratification and convective mixing of surface waters. Hence, evaporation-induced surface salinification cannot stay long. In contrast, precipitation reduces SSS. The reduced surface density increases surface buoyancy and stabilizes the upper-ocean stratification that allows the rain-induced fresher surface water to last long enough before being destroyed by other processes such as wind-induced vertical mixing. Such an effect is expected to be more significant under low-wind conditions.

Finally, it is worth pointing out that, in coastal oceans and marginal seas where in-situ measurements are sparse and where satellite SSS are subject to potential contamination by land signals, dedicated regional analyses are necessary to better understand the seasonal cycle of SSS and the potential limitations of the in-situ and satellite salinity observing systems.

Acknowledgements

L.Yu was funded by NASA Ocean Salinity Science Team (OSST) activities through Grant 80NSSC18K1335. FMB was funded by the NASA OSST through grant 80NSSC18K1322. E. P. Dinnat was funded by NASA through grant 80NSSC18K1443. Data producers for the following satellite SSS datasets are sincerely thanked: CNES-IFREMER Centre Aval de Traitement des Données SMOS (CATDS) for the SMOS LOCEAN L3 Debiased products (https://www.catds.fr/Products/Available-products-from-CEC-OS/CEC-Locean-L3-Debiased-v4), the Barcelona Expert Center (BEC) for the SMOS BEC global SSS products (http://bec.icm.csic.es/ocean-global-sss/), the SMAP JPL and RSS products (https://podaac.jpl.nasa.gov/SMAP). We also acknowledge the following in situ gridded products: Argo (http://sio-argo.ucsd.edu/RG_Climatology.html) and EN4 (https://www.metoffice.gov.uk/ hadobs/en4/).

References

Alory, G., C. Maes, T. Delcroix, N. Reul, and F. Illig, 2012. Seasonal dynamics of sea surface salinity off Panama: The far Eastern Pacific Fresh Pool, *J. Geophys. Res. Oceans*, **117**, C04028, doi:10.1029/2011JC007802.

Bingham, F. M., G. R. Foltz, M. J. McPhaden, 2010. Seasonal cycles of surface layer salinity in the Pacific Ocean. *Ocean Sci*., **6**, 775–787, https://doi.org/10.5194/os-6-775-2010.

Bingham, F. M., G. R. Foltz, and M. J. McPhaden, 2012. Characteristics of the seasonal cycle of surface layer salinity in the global ocean. *Ocean Science*, **8**(5), 915.

Bingham, F. M. and T. Lee, 2017. Space and time scales of sea surface salinity and freshwater forcing variability in the global ocean (60°S– 60°N). *J. Geophys. Res. Oceans*, **122**, 2909–2922, doi:10.1002/ 2016JC012216.

Boutin, J., P. Waldteufel, N. Martin, G. Caudal, E. Dinnat, 2004. Salinity retrieved from SMOS measurements over Global Ocean: Imprecisions due to surface roughness and temperature uncertainties. *J. Atmos. Ocean. Technol.*, **21**, 1432–1447. doi:10.1175/1520-0426(2004)021<1432:SSRFSM>2.0.CO;2.

Boutin, J., Y. Chao, Y., W. E. Asher, *et al.* 2016. Satellite and in situ salinity: understanding near- surface stratification and sub-footprint variability. *Bull. Am. Meteorol. Soc*. **97**(10). https://doi.org/10.1175/BAMS-D-15-00032.1.

Boutin, J, J. L. Vergely, S. Marchand, F. D'Amico, A. Hasson, N. Kolodziejczyk, N. Reul, G. Reverdin, and J. Vialard, 2018. New SMOS sea surface salinity with reduced systematic errors and improved variability. *Remote Sens. Environ*. **214**, 115–134.

Boutin J., J.-L.Vergely, C. Thouvenin-Masson, A. Supply, D. Khvorostyanov, 2019. SMOS SSS L3 maps generated by CATDS CEC LOCEAN. debias V4.0. SEANOE., https://doi.org/10.17882/52804.

Boyer, T. P., and S. Levitus, 1994. Quality control and processing of historical oceanographic temperature, salinity, and oxygen data, NOAA Tech. Rep. NESDIS 81, U.S. Govt. Print. Off., Washington, D. C., 64 pp.

Boyer, T. P. and S. Levitus, 2002. Harmonic Analysis of Climatological Sea Surface Salinity. *J. Geophys. Res.*, **107**(C12), doi:10.1029/2001JC000829.

Boyer, T. P., M. E. Conkright, S. Levitus, D. Johnson, J. Antonov, T. O'Brien, C. Stephens, and R. Gelfeld, 1998. World Ocean Database 1998, vol. 5, Temporal Distribution of Ocean Station Data (Bottle) Temperature Profiles [CD-ROMs], 108 pp., NOAA Atlas NESDIS 22, U.S. Govt. Print. Off., Washington, D. C.

Bruce, J. G., G. D. R. Johnson, and J. C. Kindle, 1994. Evidence for eddy formation in the eastern Arabian Sea during the northeast monsoon. *J. Geophys. Res.*, **99**(C4): 7 651–7 664, http://dx.doi.org/10.1029/94JC00035.

Camara, I., N. Kolodziejczyk, J. Mignot, A. Lazar, and A. T. Gaye, 2015. On the seasonal variations of salinity of the tropical A tlantic mixed layer. *J. Geophys. Res. Oceans*, **120**, 4441– 4462, doi:10.1002/2015JC010865.

Chao, Y., J. D. Farrara, G. Schumann, K. M. Andreadis, D. Moller, 2015. Sea surface salinity variability in response to the Congo river discharge Cont. *Shelf Res.* **99**, 35–45. https://doi.org/10.1029/2010JC006937.

Chen, G., L. Peng, and C. Ma, 2018: Climatology and seasonality of upper ocean salinity: A three-dimensional view from Argo floats. *Clim. Dyn.*, **50,** 2169–2182. https://doi.org/10.1007/s00382-017-3742-6

Cherniavskaia, E., I. Sudakov, K. Golden, C. Strong, and L. Timokhov, 2018. Observed winter salinity fields in the surface layer of the Arctic Ocean and statistical approaches to predicting large-scale anomalies and patterns. *Annals of Glaciology*, **59**, 83-100. doi:10.1017/aog.2018.10.

D'Addezio, J. M., B. Subrahmanyam, E. S. Nyadjro, and V. S. N. Murty, 2015. Seasonal variability of salinity and salt transport in the Northern Indian ocean. *J. Phys. Oceanogr*., **45**, 1947–1966.

da Silva, C. E., and R. M. Castelao, 2018. Mississippi River plume variability in the Gulf of Mexico from SMAP and MODIS-Aqua observations. *J. Geophys. Res. Oceans*, **123**, 6620– 6638. https://doi.org/10.1029/2018JC014159

Delcroix, T. 1998. Observed surface oceanic and atmospheric variability in the tropical Pacific at sea- sonal and ENSO timescales: A tentative overview. *J. Geophys. Res.*, **103**, 18,611–18,633, https://doi.org/10.1029/98JC00814.

Delcroix, T., C. Hénin, V. Porte, and P. Arkin, 1996. Precipitation and sea-surface salinity in the tropical Pacific Ocean, *Deep-Sea Res.*, **43**, 1123– 1141.

Delcroix, T., M. J. McPhaden, A. Dessier, and Y. Gouriou, 2005. Time and space scales for sea surface salinity in the tropical oceans, *Deep-Sea Res.*, **52**(5), 787–813.

Dessier, A., and J. R. Donguy, 1994. The sea surface salinity in the tropical Atlantic between 10S and 30N – Seasonal and interannual variations (1977–1989). *Deep Sea Res., Part I*, **41**, 81–100.

Dinnat, E., D. Le Vine, J. Boutin, T. Meissner, and G. Lagerloef, 2019. Remote sensing of sea surface salinity: Comparison of satellite and in situ observations and impact of retrieval parameters. *Remote Sens.* **11**, 750. https://doi.org/10.3390/rs11070750.

Dong, S., S. L. Garzoli, and M. Baringer, 2009. An assessment of the seasonal mixed layer salinity budget in the Southern Ocean. *J. Geophys. Res. Oceans*, **114**, C12001. https://doi.org/10.1029/2008JC005258

Donguy, J. E., and G. Meyers, 1996. Seasonal variations of sea surface salinity and temperature in the tropical Indian Ocean. *Deep Sea Res., Part I*, **43**, 117– 138.

Drucker, R., and S. C. Riser, 2014. Validation of Aquarius sea surface salinity with Argo: Analysis of error due to depth of measurement and vertical salinity stratification. *J. Geophys. Res. Oceans*, **119**, 4626–4637, doi:10.1002/ 2014JC010045

Entekhabi, D., E. G. Njoku, P. E. O'Neill, *et al.* **2010**. The soil moisture active passive (SMAP) mission. *Proc. IEEE*, **98**, 704–716. doi: 10.1109/JPROC.2010.2043918.

Foltz, G. R., and M. J. McPhaden, 2008. Seasonal mixed layer salinity balance of the tropical North Atlantic Ocean, *J. Geophys. Res.*, **113**, C02013, doi:10.1029/2007JC004178.

Fore, A., S. Yueh, W. Tang, and A. Hayashi, 2020. JPL SMAP Ocean Surface Salinity Products [Level 2B, Level 3 Running 8-day, Level 3 Monthly], Version 4.3 validated release. Jet Propulsion Laboratory, Pasadena, CA, USA.

Fournier, S., T. Lee, and M. M. Gierach, 2016. Seasonal and interannual variations of sea surface salinity associated with the Mississippi River plume observed by SMOS and Aquarius. *Remote Sens. Environ.*, **180**, 431-439.

Fournier, S., J. Vialard, M. Lengaigne, T. Lee, M. Gierach, 2017a. Modulation of the Ganges-Brahmaputra river plume by the Indian Ocean Dipole and eddies inferred from satellite observations. *J. Geophys. Res. Oceans*, **122**. https:// doi.org/10.1002/2017JC013333.

Fournier, S., D. Vandemark, L. Gaultier, T. Lee, B. Jonsson, M. Gierach, 2017b. Interannual variation in offshore advection of Amazon-Orinoco plume waters: observations, forcing mechanisms, and impacts. *J. Geophys. Res. Oceans*, **122**. https://doi.org/10.1002/2017JC013103.

Fournier, S., T. Lee, W. Tang, M. Steele, E. Olmedo, 2019. Evaluation and intercomparison of SMOS, Aquarius, and SMAP sea surface salinity products in the Arctic Ocean. *Remote Sens.* **11**, 3043, doi:10.3390/rs11243043.

Garcia-Eidell, C., J. C. Comiso, E. Dinnat, and L. Brucker, 2017. Satellite observed salinity distributions at high latitudes in the Northern Hemisphere: A comparison of four products. *J. Geophys. Res. Oceans*, **122**(9), 7717–7736. https://doi.org/10.1002/2017JC013184.

Garcia-Eidell, C., J. C. Comiso, E. Dinnat, and L. Brucker, 2019. Sea surface salinity distribution in the southern ocean as observed from space. *J. Geophys. Res. Oceans*, **124**(5), 3186–3205. https://doi.org/10.1029/2018JC014510.

Gelderloos, R., F. Straneo, and C. A. Katsman, 2012: Mechanisms behind the Temporary Shutdown of Deep Convection in the Labrador Sea: Lessons from the Great Salinity Anomaly Years 1968–71. *J. Climate*, **25**, 6743–6755, https://doi.org/10.1175/JCLI-D-11-00549.1.

Gierach, M., J. Vazquez-Cuervo, T. Lee, V. M. Tsontos, 2013. Aquarius and SMOS detect effects of an extreme Mississippi River flooding event in the Gulf of Mexico. *Geophys. Res. Lett.* **40**(19), 5188–5193. https://doi.org/10.1002/grl.50995.

Good, S. A., M. J. Martin, and N. A. Rayner, 2013. EN4: Quality controlled ocean temperature and salinity profiles and monthly objective analyses with uncertainty estimates. *J. Geophys. Res. Oceans*, **118**, 6704– 6716. https://doi.org/10.1002/2013JC009067.

Gordon, A.L., C.F. Giulivi, J. Busecke, and F.M. Bingham. 2015. Differences among subtropical surface salinity patterns. *Oceanography*, **28**(1):32–39, https://doi.org/ 10.5670/oceanog.2015.02.

Greene, C. H., 2013. Towards a more balanced view of marine ecosystems. *Fish Oceanogr*, **22**, 140-142. doi:10.1111/fog.12006.

Grodsky, S.A., G. Reverdin, J. A. Carton, V. J. Coles, 2014. Year-to-year salinity changes in the Amazon plume: contrasting 2011 and 2012 Aquarius/SAC-D and SMOS satellite data. *Remote Sens. Environ.* **140**, 14–22. https://doi.org/10.1016/j.rse.2013. 08.033.

Grodsky, S.A., N. Reul, B. Chapron, J. A. Carton, and F. O. Bryan, 2017. Interannual surface salinity in Northwest Atlantic shelf. *J. Geophys. Res. Oceans,* **122**(5), 3638–3659.

Guimbard, S., N. Reul, B. Chapron, M. Umbert, and C. Maes. 2017. Seasonal and interannual vari- ability of the Eastern Tropical Pacific Fresh Pool. *J. Geophys. Res. Oceans,* **122**, 1,749–1,771, https://doi.org/10.1002/2016JC012130.

Hasson, A. E. A., T. Delcroix, and R. Dussin, 2013a. An assessment of the mixed layer salinity budget in the tropical Pacific Ocean: Observations and modelling (1990–2009). *Ocean Dyn.*, **63**(2–3), 179– 194, doi:10.1007/s10236-013-0596-2.

Hasson, A., T. Delcroix, and J. Boutin, 2013b. Formation and variability of the South Pacific Sea Surface Salinity maximum in recent decades. *J. Geophys. Res. Oceans,* **118**, doi:10.1002/jgrc.20367

Henocq, C., J. Boutin, G. Reverdin, F. Petitcolin, S. Arnault, and P. Lattes, 2010. Vertical Variability of Near-Surface Salinity in the Tropics: Consequences for L-Band Radiometer Calibration and Validation. *J. Atmos. Oceanic Technol.*, **27**, 192–209, https://doi.org/10.1175/2009JTECHO670.1

Jensen, T. G. 2001. Arabian Sea and Bay of Bengal exchange of salt and tracers in an ocean model, *Geophys. Res. Lett.*, **28**(20), 3967– 3970.

Jensen, M.F., J. Nilsson, and K. H. Nisancioglu, 2016. The interaction between sea ice and salinity-dominated ocean circulation: implications for halocline stability and rapid changes of sea ice cover. *Clim Dyn* **47,** 3301–3317. https://doi.org/10.1007/s00382-016-3027-5.

Johnson, B.K., F.O. Bryan, S.A. Grodsky, and J.A. Carton, 2016: Climatological Annual Cycle of the Salinity Budgets of the Subtropical Maxima. *J. Phys. Oceanogr.*, **46**, 2981–2994, https://doi.org/10.1175/JPO-D-15-0202.1.

Kerr, Y. H., P. Waldteufel, J.-P. Wigneron, *et al*. 2010. The SMOS L: New tool for monitoring key elements of the global water cycle. Proc. IEEE, **98**(5), 666-687. doi:10.1109/JPROC.2010.2043032.

Köhler, J., M.S. Martins, N. Serra, D. Stammer, 2015. Quality assessment of spaceborne sea surface salinity observations over the northern North Atlantic. *J. Geophys. Res. Oceans*, **120**, 94–112, doi:10.1002/2014JC010067.

Lagerloef, G., C. Swift, D. Le Vine, 1995. Sea surface salinity: the next remote sensing challenge. *Oceanography*, **8**(2), 44–50.

Le Vine, D., A. Saji, Y. H. Kerr, W. J. Wilson, N. Skou, S. Sobjaerg, 2005. Comparison of model predictions with measurements of galactic background noise at L-band. *IEEE Geosci. Remote Sens.*, **43**(9), 2018–2023. doi:10.1109/TGRS.2005.853190.

Levitus, S., 1986. Annual cycle of salinity and salt storage in the world ocean. *J. Phys. Oceanogr.*, **16**, 322–343.

Maes, C., and T. J. O'Kane, 2014. Seasonal variations of the upper ocean salinity stratification in the Tropics, *J. Geophys. Res. Oceans*, **119**, 1706– 1722, doi:10.1002/2013JC009366.

Martín-Neira, M., R. Oliva, I. Corbella, et al. 2016. SMOS instrument performance and calibration after six years in orbit. *Remote Sens. Environ.*, **180**, 19–39. https://doi.org/10.1016/j.rse.2016.02.036

Melnichenko, O.V., P. Hacker, F. Bingham, T. Lee, 2019. Patterns of SSS variability in the eastern tropical Pacific: intra-seasonal to inter-annual time-scales from seven years of NASA satellite data. *Oceanography*, **32**(2), 20-29, doi:10.5670/oceanog.2019.208.

Meissner, T., F. J. Wentz, A. Manaster, 2018: NASA/RSS SMAP Salinity: Version 3.0 Validated Release, Release Notes, Algorithm Theoretical Basis Document (ATBD), Validation, Data Format Specification. RSS Technical Report 091316. Available at http://data.remss.com/smap/SSS/Release_V4.0.pdf

Meissner, T., F. J. Wentz, A. Manaster, R. Lindsley, 2019: Remote Sensing Systems SMAP Ocean Surface Salinities [Level 2C, Level 3 Running 8-day, Level 3 Monthly], Version 4.0 validated release. Remote Sensing Systems, Santa Rosa, CA, USA. Available online at www.remss.com/missions/smap.

Melzer, B. A., and B. Subrahmanyam, 2015. Investigating decadal changes in sea surface salinity in oceanic subtropical gyres. *Geophys. Res. Lett.*, **42**, 7631–7638, doi:10.1002/2015GL065636.

Momin, I. M., A. K. Mitra, S. Prakash, D. K. Mahapatra, A. Gera, and E. N. Rajagopal, 2015. Variability of sea surface salinity in the tropical Indian Ocean as inferred from Aquarius and in situ data sets. *Int. J. Remote Sens.*, **36**(7), 1907-1920.

Oliva, R., E. Daganzo-Eusebio, Y.H. Kerr, *et al*. 2012. SMOS radio frequency interference scenario: status and actions taken to improve the RFI environment in the 1400-1427- MHz passive band. *IEEE Trans. Geosci. Remote Sens.*, **50**(5), 1427-1439, doi:10.1109/TGRS.2012.2182775.

Olmedo, E., J. Martínez, A. Turiel, J. Ballabrera-Poy, M. Portabella, 2017. Debiased non-Bayesian retrieval: A novel approach to SMOS Sea Surface Salinity. *Remote Sens. Environ.*, **193**, 103-126, /doi:10.1016/j.rse.2017.02.023.

Piepmeier, J. R., J. T. Johnson, P. N. Mohammed, D. Bradley, C. Ruf, M. Aksoy, R. Garcia, D. Hudson, L. Miles, and M. Wong, 2014. Radio-frequency Interference Mitigation for the Soil Moisture Active Passive Microwave Radiometer. *IEEE Trans. Geosci. Remote Sen.* **52**(1), 761-775.

Piola, A. R., R. P. Matano, E. D. Palma, O. O. Möller, and E. J. D. Campos, 2005. The influence of the Plata River discharge on the western South Atlantic shelf. *Geophys. Res. Lett.*, **32**, L01603, doi:10.1029/2004GL021638.

Piracha, A., R. Sabia, M. Klockmann, L. Castaldo, and D. Fernández, 2019. Satellite-driven estimates of water mass formation and their spatio-temporal evolution. *Front. Mar. Sci.*, **6**(589), doi:10.3389/fmars.2019.00589.

Rao, R. R., and R. Sivakumar, 2003. Seasonal variability of sea surface salinity and salt budget of the mixed layer of the north Indian Ocean. *J. Geophys. Res. Oceans*, **108**(C1), 3009, https://doi.org/10.1029/2001JC000907.

Reagan, J., T. Boyer, J. Antonov, and M. Zweng, 2014. Comparison analysis between Aquarius sea surface salinity and World Ocean Database in situ analyzed sea surface salinity. *J. Geophys. Res. Oceans*, **119**, 8122– 8140, doi:10.1002/2014JC009961.

Ren, L., K. Speer, and E. P. Chassignet, 2011. The mixed layer salinity budget and sea ice in the Southern Ocean, *J. Geophys. Res.*, **116**, C08031, doi:10.1029/2010JC006634.

Reul, N., J. Tenerelli, B. Chapron, P. Waldteufel, 2007. Modelling sun glitter at L-band for the sea surface salinity remote sensing with SMOS. *IEEE Trans. Geosci. Remote Sens.*, **45**(7), 2073–2087. doi: 10.1109/TGRS.2006.890421.

Reul, N., Fournier, S., Boutin, J., Hernandez, O., Maes, C., Chapron, B., Alory, G., Quilfen, Y., Tenerelli, J., Morisset, S., Kerr, Y., Mecklenburg, S., Delwart, S., 2014. Sea sur- face salinity observations from space with the SMOS satellite: A new means to monitor the marine branch of the water cycle. *Surv. Geophys.* **35**(3), 681–722. https://doi.org/10.1007/s10712-013-9244-0.

Reul, N.. S. A. Grodsky, M. Arias, *et al.* 2020. Sea surface salinity estimates from spaceborne L-band radiometers: An overview of the first decade of observation (2010–2019). *Remote Sens. Environ.*, **242**, 111769, https://doi.org/10.1016/j.rse.2020.111769.

Roemmich, D., and J. Gilson, 2009. The 2004–2008 mean and annual cycle of temperature, salinity, and steric height in the global ocean from the Argo Program. *Prog. Oceanogr.*, **82**, 81–100.

Sasamal, S. K., 1990. High saline waters in Bay of Bengal. *Proc. Indian Acad. Sci. (Earth. Planet. Sci.)*, **99**, 367-381.

Schanze, J. J., R. W. Schmitt, and L. L. Yu, 2010. The global oceanic freshwater cycle: A state-of-the-art quantification. *J. Mar. Res.*, **68**(3), 569–595, doi:10.1357/002224010794657164.

Schmidtko, S., G. C. Johnson, and J. M. Lyman, 2013. MIMOC: A global monthly isopycnal upper-ocean climatology with mixed layers, J. *Geophys. Res. Oceans*, **118**, 1658–1672, doi:10.1002/jgrc.20122

Schmitt, R.W., 2008. Salinity and the global water cycle. *Oceanography*, **21**(1), 12–19. https://doi.org/10.5670/oceanog.2008.63.

Schott F, & McCreary J P. 2001. The monsoon circulation of the Indian Ocean. *Prog. Oceanogr.*, **51**(1), 1–123, http://dx.doi.org/10.1016/S0079-6611(01)00083-0.

Shenoi, S. S. C., D. Shankar, and S. R. Shetye, 1999. On the sea surface temperature high in the Lakshadweep Sea before the onset of the southwest monsoon, *J. Geophys. Res.*, **104**(C7), 15703– 15712, doi:10.1029/1998JC900080.

SMOS-BEC Team, 2019: Global SMOS-BEC Debiased non-Bayesian SSS L3 and L4 Product Description. Barcelona Expert Centre, Spain, Technical note: BEC-SMOS-0007-QR version 1.0, available at: http://bec.icm.csic.es/doc/BEC-SMOS-0002-PD-SSS-Global.pdf, BEC 2019-07-15. Issue 1.0. pp.25.

Swift, C. T. 1980. Passive microwave remote sensing. *Bound.-Layer Meteor.*, **18,** 25–54.

Swift, C.T., McIntosh, R.E., 1983. Considerations for microwave remote sensing of ocean surface salinity. *IEEE Trans. Geosci. Remote Sens*. **21**, 480–491.

Talley, L.D. 2002. Salinity patterns in the ocean. In *Encyclopedia of Global Environmental Change (vol. 1): The Earth System.* Physical and Chemical Dimensions of Global Environmental Change. M.C. MacCracken and J.S. Perry, eds, John Wiley and Sons. pp. 629–640.

Tang, W., S. Yueh, D. Yang, A. Fore, A. Hayashi, T. Lee, S. Fournier, and B. Holt, 2018. The potential and challenges of using SMAP SSS to monitor Arctic Ocean freshwater changes. *Remote Sens.*, doi:10.3390/rs10060869, June 2018.

Tang, W.; Yueh, S.H.; Yang, D.; Mcleod, E.; Fore, A.; Hayashi, A.; Olmedo, E.; Martínez, J.; and Gabarró, C. 2020. The Potential of Space-Based Sea Surface Salinity on Monitoring the Hudson Bay Freshwater Cycle. *Remote Sens.* **12**, 873, doi:10.3390/rs12050873.

Vinayachandran, P. N., D. Shankar, S. Vernekar, K. K. Sandeep, P. Amol, C. P. Neema, and A. Chatterjee, 2013. A summer monsoon pump to keep the Bay of Bengal salty. *Geophys. Res. Lett.*, **40**, 1777–1782, doi:10.1002/grl.50274.

Vinogradova, N., L. Tong, J. Boutin, *et al.* 2019. Satellite salinity observing system: Recent discoveries and the way forward. *Front. Mar. Sci.*, **6**, 243, doi:10.3389/fmars.2019.00243.

Vinogradova, N. T., and R. M. Ponte, 2013. Clarifying the link between surface salinity and freshwater fluxes on monthly to interannual time scales. *J. Geophys. Res. Oceans*, **118**, 3190– 3201. https://doi.org/10.1002/jgrc.20200.

Wilks, D.S. (1995) Statistical Methods in the Atmospheric Sciences. Academic Press, San Diego, 467 pp.

Wyrtki, K. 1965. The annual and semiannual variation of sea surface temperature in the North Pacific Ocean. *Limnol. Oceanogr.*, **10**, 307-313, doi: 10.4319/lo.1965.10.3.0307.

Yu, L. 2010. On Sea Surface Salinity Skin Effect Induced by Evaporation and Implications for Remote Sensing of Ocean Salinity. *J. Phys. Oceanogr.* **40,** 85–102, doi:10.1175/2009JPO4168.1.

Yu, L. 2011. A global relationship between the ocean water cycle and near-surface salinity. *J. Geophys. Res. Oceans*, **116**, C10025. https://doi.org/10.1029/2010JC006937

Yu, L., 2015. Sea-surface salinity fronts and associated salinity-minimum zones in the tropical ocean. *J. Geophys. Res. Oceans*, **120**(6), 4205–4225. doi:10.1002/2015JC010790.

Yu, L., Jin, X., Liu, H., 2018. Poleward shift in ventilation of the North Atlantic sub- tropical underwater. *Geophys. Res. Lett*. **45**, 258–266. https://doi.org/10.1002/ 2017GL075772.

Yu, L., 2012. Variability and Uncertainty of Satellite Sea Surface Salinity in the Subpolar North Atlantic (2010–2019). *Remote Sens.* **12**(13), 2092. https://doi.org/10.3390/rs12132092.

Yu, L., S.A. Josey, F.M. Bingham, and T. Lee, 2020. Intensification of the global water cycle and evidence from ocean salinity: a synthesis review. *Ann. N.Y. Acad. Sci.*, **1472**, 76-94. doi:10.1111/nyas.14354.

Yueh, S.H., West, R., Wilson, W.J., Li, F.K., Njoku, E.G., Rahmat-Samii, Y., 2001. Error sources and feasibility for microwave remote sensing of ocean salinity. *IEEE Trans. Geosci. Remote Sens.* **39**(5), 1049–1060.

List of Tables

Table 1. Main characteristics of the six products used in the study

Data Products	Version	Start Time	Resolution	Reference
SMAP JPL	v4.3	APR 2015	0.25°, monthly and 8-day running mean	Fore et al. (2016; 2019) https://podaac.jpl.nasa.gov/SMAP
SMAP RSS	v4.0	APR 2015	0.25°, monthly and 8-day running mean; 40-km and 70-km maps	Meissner et al. (2019a;b) https://podaac.jpl.nasa.gov/SMAP
SMOS LOCEAN	De-biased v4	JAN 2010	0.25°, 9-day and 18-day averaged mean	Boutin et al. (2018; 2019) ftp://ext-catds-cecos-locean:catds2010@ftp.ifremer.fr/
SMOS BEC	v2	FEB 2011	0.25°, Daily from 9 day objective analysis	Olmedo et al. (2017) sftp://becftp.icm.csic.es:27500
Argo	v2019	JAN 2004	1°, monthly	Roemmich and Gilson (2009) http://sio-argo.ucsd.edu/RG_Climatology.html
EN4	V4.2.1	JAN 1900	1°, monthly	Good et al. (2013) https://www.metoffice.gov.uk/hadobs/en4

Table 2. Locations and abbreviated names of the nine boxes shown in Figure 2, along with product ensemble SSS mean and STD (spread) within the box.

Regime	**Box number**	**Abbreviated Name**	**Location**	**Mean SSS**
Smin Tropical	Box 1	Smin-Pac	5–15°N, 155–100°W	33.84 ± 0.09
	Box 2	Smin-Atl	3–13°N, 42–17°W	35.69 ± 0.03
	Box 3	Smin-BoB	5–20°N, 82–92°E	32.93 ± 0.07
Smax Northern Hemisphere Subtropical	Box 4	Smax-NPac	22–32°N, 160–220°E	35.12 ± 0.02
	Box 5	Smax-NAtl	20–30°N, 55–15°W	37.24 ± 0.03
	Box 6	Smax-AS	5–22°N, 55–70°E	36.16 ± 0.13
Smax Southern Hemisphere Subtropical	Box 7	Smax-SPac	14–24°S, 210–265°E	36.25 ± 0.03
	Box 8	Smax-SAtl	13–23°S, 38–18°W	37.16 ± 0.03
	Box 9	Smax-SInd	25–35°S, 60–110°E	35.70 ± 0.04

Table 3. Percentage of the total variance explained by the annual and semiannual harmonics and the reconstructed seasonal cycle for the global ocean and the three basins

Basin	Harmonic Mode	SMAP JPL	SMP RSS	SMOS LOCEAN	SMOS BEC	Argo	EN4
Global (50°S-50°N)	Ann | Semi	53 | 9	76 | 12	73 | 14	42 | 7	75 | 12	84 | 11
	Reconstructed	**62**	**88**	**86**	**49**	**87**	**95**
Pacific	Ann | Semi	34 | 7	71 | 13	66 | 15	23 | 6	76 | 12	85 | 10
	Reconstructed	**41**	**83**	**81**	**29**	**88**	**95**
Atlantic	Ann | Semi	61 | 9	79 | 10	79 | 11	74 | 9	76 | 11	85 | 10
	Reconstructed	**70**	**89**	**90**	**83**	**87**	**95**
Indian	Ann | Semi	70 | 13	78 | 14	73 | 16	76 | 13	72 | 15	82 | 13
	Reconstructed	**83**	**92**	**89**	**89**	**87**	**95**

Table 4. Amplitudes of the annual (A1) and semiannual (A2) harmonics in the nine boxes for different products and the ensemble mean.

<table>
<tr><th rowspan="2">Regime</th><th rowspan="2">Box Number</th><th>SMAP JPL</th><th>SMP RSS</th><th>SMOS LOCEAN</th><th>SMOS BEC</th><th>Argo</th><th>EN4</th><th>Ensemble Mean</th></tr>
<tr><th>A_1 | A_2</th><th>A_1 | A_2</th><th>A_1 | A_2</th><th>A_1 | A_2</th><th>A_1 | A_2</th><th>A_1 | A_2</th><th>A_1 | A_2</th></tr>
<tr><td rowspan="3">Smin
Tropical regime</td><td>Box 1
Smin-Pac</td><td>0.24 | 0.05</td><td>0.25 | 0.05</td><td>0.24 | 0.05</td><td>0.17 | 0.02</td><td>0.26 | 0.05</td><td>0.23 | 0.03</td><td>0.23 ± 0.03 |
0.04 ± 0.01</td></tr>
<tr><td>Box 2
Smin-Atl</td><td>0.33 | 0.07</td><td>0.31 | 0.07</td><td>0.38 | 0.07</td><td>0.21| 0.01</td><td>0.28| 0.08</td><td>0.26| 0.06</td><td>0.30 ± 0.06 |
0.06 ± 0.03</td></tr>
<tr><td>Box 3
Smin-BoB</td><td>0.33 | 0.20</td><td>0.24 | 0.21</td><td>0.32 | 0.15</td><td>0.37 | 0.12</td><td>0.21 | 0.21</td><td>0.18 | 0.14</td><td>0.28 ± 0.08 |
0.17 ± 0.04</td></tr>
<tr><td rowspan="3">Smax
NH regime</td><td>Box 4
Smax-NPac</td><td>0.08 | 0.01</td><td>0.01 | 0.02</td><td>0.02 | 0.06</td><td>0.01 | 0.03</td><td>0.04 | 0.01</td><td>0.02 | 0.01</td><td>0.03 ± 0.03 |
0.02 ± 0.02</td></tr>
<tr><td>Box 5
Smax-NAtl</td><td>0.12 | 0.01</td><td>0.04 | 0.02</td><td>0.03 | 0.02</td><td>0.00 | 0.01</td><td>0.06 | 0.02</td><td>0.06 | 0.02</td><td>0.05 ± 0.04 |
0.02 ± 0.01</td></tr>
<tr><td>Box 6
Smax-AS</td><td>0.23 | 0.09</td><td>0.24 | 0.06</td><td>0.17 | 0.05</td><td>0.11 | 0.04</td><td>0.20 | 0.08</td><td>0.21 | 0.07</td><td>0.19 ± 0.05 |
0.07 ± 0.02</td></tr>
<tr><td rowspan="3">Smax
SH regime</td><td>Box 7
Smax-SPac</td><td>0.06 | 0.02</td><td>0.04 | 0.02</td><td>0.05 | 0.00</td><td>0.03 | 0.01</td><td>0.04 | 0.01</td><td>0.02 | 0.01</td><td>0.04 ± 0.01 |
0.01 ± 0.01</td></tr>
<tr><td>Box 8
Smax-SAtl</td><td>0.16 | 0.03</td><td>0.11 | 0.01</td><td>0.10 | 0.01</td><td>0.03 | 0.01</td><td>0.10 | 0.01</td><td>0.08 | 0.00</td><td>0.10 ± 0.04 |
0.01 ± 0.01</td></tr>
<tr><td>Box 9
Smax-SInd</td><td>0.05 | 0.03</td><td>0.07 | 0.03</td><td>0.03 | 0.05</td><td>0.04 | 0.01</td><td>0.05 | 0.00</td><td>0.05 | 0.02</td><td>0.05 ± 0.01 |
0.02 ± 0.02</td></tr>
</table>

Table 5. Major features of the reconstructed seasonal cycles in the nine boxes showing the maximum and minimum and the correlation (“corr”) with the Argo dataset.

Regime	Box Number	Amp Corr w/Argo	SMAP JPL	SMP RSS	SMOS LOCEAN	SMOS BEC	Argo	EN4	Ensemble Mean
Smin Tropical regime	Box 1 Smin-Pac	Max | Min	0.27 | −0.25	0.29 | −0.25	0.28 | −0.23	0.19 | −0.15	0.26 | −0.27	0.23 | −0.24	0.25 ± 0.04 | −0.23 ± 0.04
		Corr	1.0	0.99	0.99	0.93		1.0	
	Box 2 Smin-Atl	Maxi | Min	0.34 | −0.37	0.33 | −.34	0.40 | −.040	0.20 | −0.22	0.31 | −0.32	0.27 | −0.29	0.31 ± 0.07 | −0.32 ± 0.06
		Corr	1.0	0.99	0.99	0.96		1.0	
	Box 3 Smin-BoB	Max | Min	0.35 | −0.53	0.32 | −0.45	0.31 | −0.46	0.40 | −0.44	0.38 | −0.34	0.29 | −0.28	0.34 ± 0.04 | −0.42 ± 0.09
		Corr	0.83	0.87	0.79	0.83		0.97	
Smax NH regime	Box 4 Smax-NPac	Max | Min	0.09 | −0.08	0.02 | −0.02	0.08 | −0.07	0.04 | −0.04	0.05 | −0.04	0.03 | −0.02	0.05 ± 0.03 | −0.05 ± 0.03
		Corr	0.98	**0.48**	**−0.08**	**0.03**		0.94	
	Box 5 Smax-NAtl	Max | Min	0.12 | −0.13	0.03 | −0.05	0.04 | −0.05	0.01 | −0.01	0.07 | −0.08	0.07 | −0.07	0.06 ± 0.04 | −0.07 ± 0.04
		Corr	0.93	0.81	**0.44**	**−0.25**		0.99	
	Box 6 Smax-AS	Max | Min	0.23 | −0.31	0.19 | −0.30	0.19 | −0.20	0.15 | −0.08	0.16 | −0.28	0.17 | −0.28	0.18 ± 0.03 | −0.24 ± 0.09
		Corr	0.96	0.95	0.76	**0.44**		1.0	
Smax SH regime	Box 7 Smax-SPac	Max | Min	0.07 | −0.07	0.03 | −0.06	0.05 | −0.04	0.04 | −0.04	0.04 | −0.04	0.03 | −0.02	0.04 ± 0.02 | −0.05 ± 0.02
		Corr	0.79	0.60	0.97	**0.40**		0.88	
	Box 8 Smax-SAtl	Max | Min	0.18 | −0.16	0.10 | −0.12	0.11 | −0.09	0.04 | −0.04	0.11 | −0.09	0.08 | −0.08	0.10 ± 0.05 | −0.10 ± 0.04
		Corr	0.96	0.94	0.94	0.6		0.97	
	Box 9 Smax-SInd	Max | Min	0.07 | −0.07	0.07 | −0.09	0.07 | −0.08	0.04 | −0.05	0.04 | −0.05	0.05 | −0.05	0.06 ± 0.02 | −0.05 ± 0.02
		Corr	0.86	0.82	**0.36**	0.68		0.99	

Figure Captions

Figure 1. Figure 1. Time-mean SSS fields averaged over the period 2016-2018. (a) SMAP JPL, (b) SMAP RSS, (c) SMOS LOCEAN, (d) SMOS BEC, (e) Argo, and (f) EN4. The 35 pss is drawn (thin gray contour).

Figure 2. (a) Ensemble mean and (b) Standard deviation (STD) of the six mean SSS products. Numbered boxes are ones discussed in the text (e.g. Table 2). In (a), salinity value near each box is the product ensemble mean. Closed contours in boxes 4-9 are of the product ensemble mean shown near each box with each color denoting a different product.

Figure 3. Difference between mean SSS fields and the Argo mean. (a) SMAP JPL – Argo, (b) SMAP RSS – Argo, (c) SMOS LOCEAN – Argo, (d) SMOS BEC – Argo, (e) Argo – Argo, and (f) EN4 – Argo. In (a)-(d), the satellite products were regridded onto the Argo 1°x1° grid.

Figure 4. Standard deviation (in pss) of monthly-mean SSS based on (a) SMAP JPL, (b) SMAP RSS, (c) SMOS LOCEAN, (d) SMOS BEC, (e) Argo, and (f) EN4.

Figure 5. Amplitude of the estimated annual harmonic (in pss) for (a) SMAP JPL, (b) SMAP RSS, (c) SMOS LOCEAN, (d) SMOS BEC, (e) Argo, and (f) EN4.

Figure 6. Phase of the estimated annual harmonic for (a) SMAP JPL, (b) SMAP RSS, (c) SMOS LOCEAN, (d) SMOS BEC, (e) Argo, and (f) EN4. The month shown indicates when maximum SSS is reached in the annual cycle.

Figure 7. Same as Figure 5 but for the estimated semiannual harmonic.

Figure 8. Same as Figure 6 but for the estimated semiannual harmonic.

Figure 9. Percentage of total variance explained by the annual harmonic.

Figure 10. Same as Figure 9 but for the reconstructed seasonal cycle.

Figure 11. (left) annual cycle, (center) semiannual cycle, and (right) combined annual and semiannual cycle averaged over (a) Box 1 (Smin-Pac), (b) Box 2 (Smin-Atl), and (c) Box 3 (Smin-BoB).

Figure 12. Same as Figure 11 but for (a) Box 4 (Smax-NPac), (b) Box 5 (Smax – NAtl), and (c) Box 6 (Smax – AS).

Figure 13. Same as Figure 11 but for (a) Box 7 (Smax-SPac), (b) Box 8 (Smax – SAtl), and (c) Box 9 (Smax – SInd).

Figure 14. The seasonal cycle of the reconstructed time series averaged over the five subtropical salinity maximum centers bounded by a fixed box (red line) and by the selected isohaline (blue line). The lighter color shading denotes one standard deviation between six products.

Figure 15. Summary of the mean and standard error (bold-face numbers) as well as the seasonal ranges (light-face numbers) for each boxed region. The mean and standard error were computed as the product ensemble mean and spread (STD) (see Table 2). The seasonal ranges were based on the maximum and minimum estimated from the reconstructed time series averaged over the nine selected boxes (see Table 5).

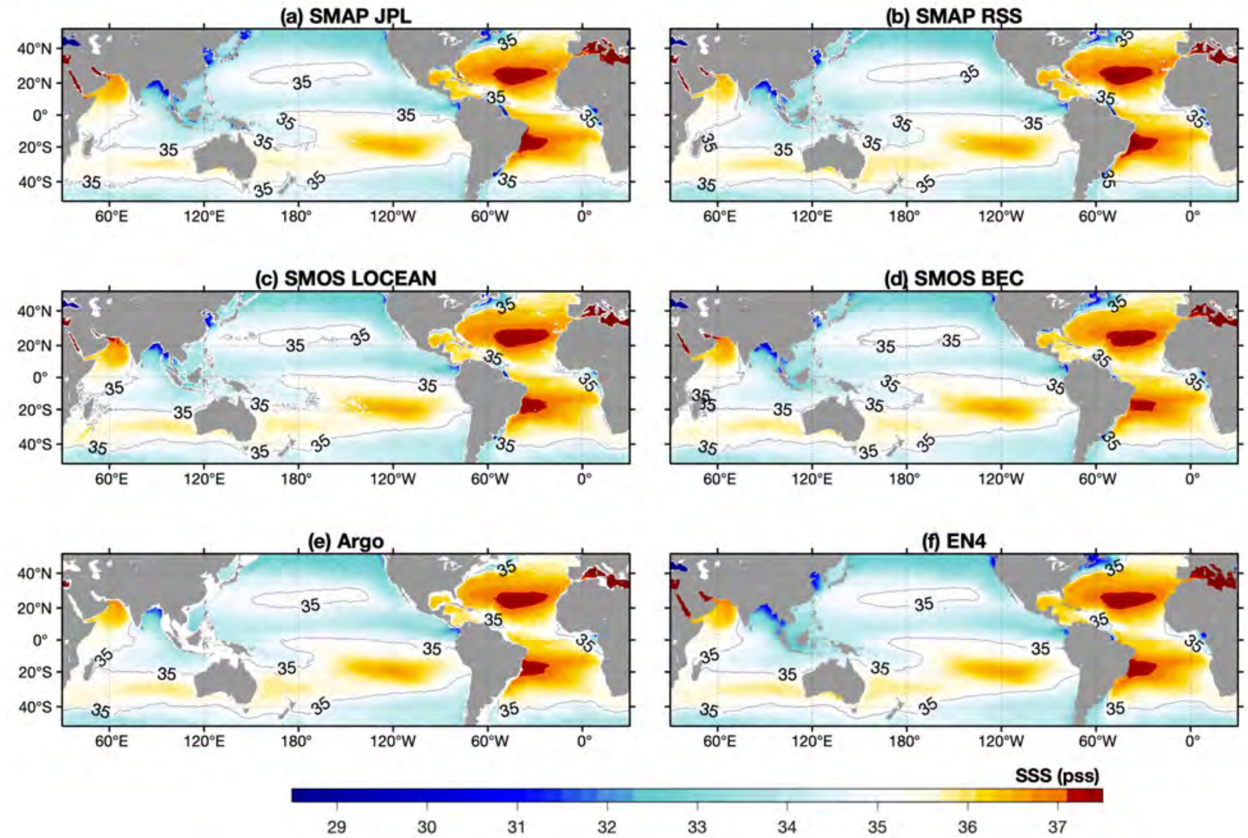

Figure 1. Time-mean SSS fields averaged over the period 2016-2018. (a) SMAP JPL, (b) SMAP RSS, (c) SMOS LOCEAN, (d) SMOS BEC, (e) Argo, and (f) EN4. The isohaline of 35 pss is drawn (thin gray contour).

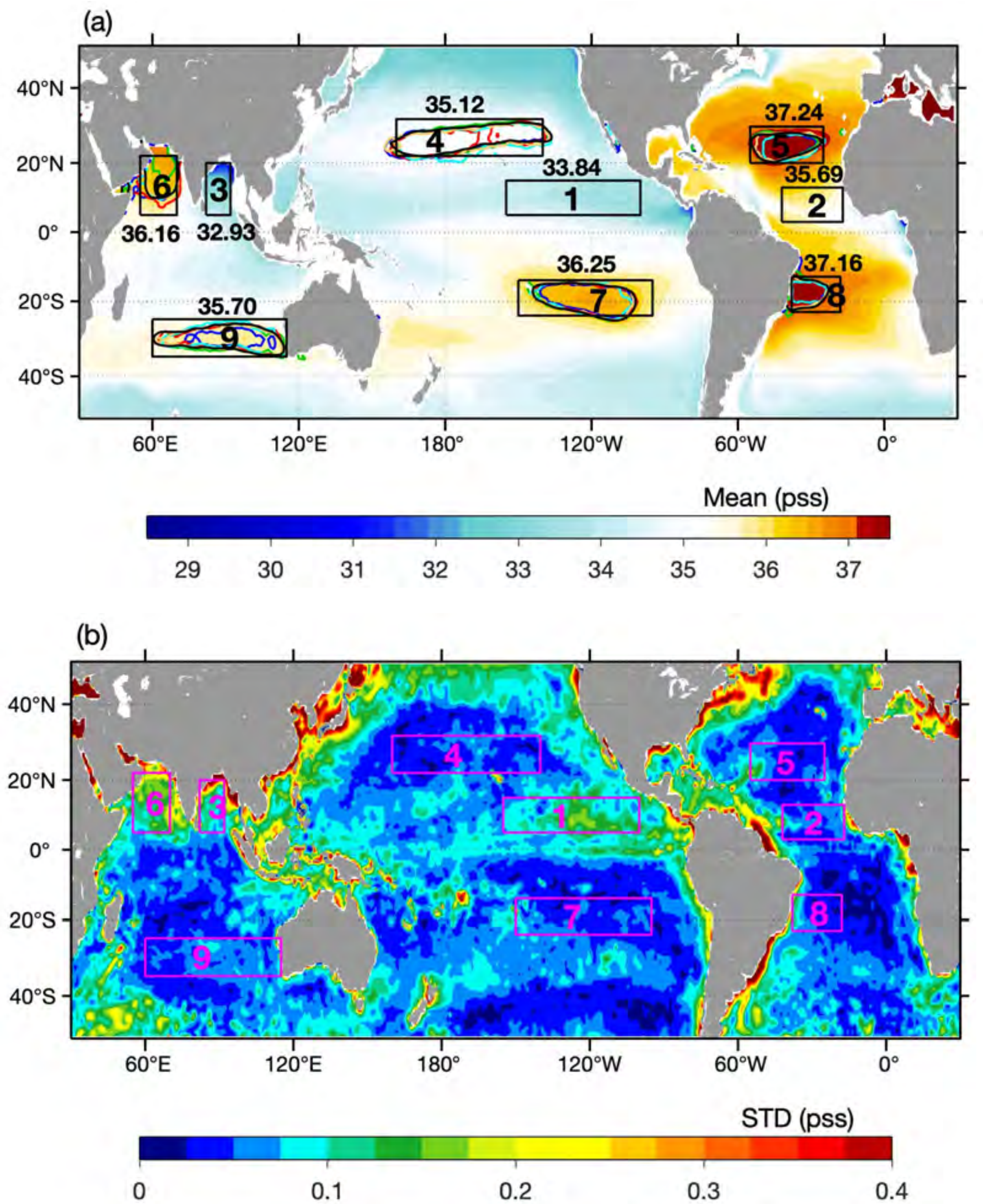

Figure 2. (a) Ensemble mean and (b) Standard deviation (STD) of the six mean SSS products. Numbered boxes are ones discussed in the text (e.g. Table 2). In (a), salinity value near each box is the product ensemble mean. Closed contours in boxes 4-9 are of the product ensemble mean shown near each box with each color denoting a different product.

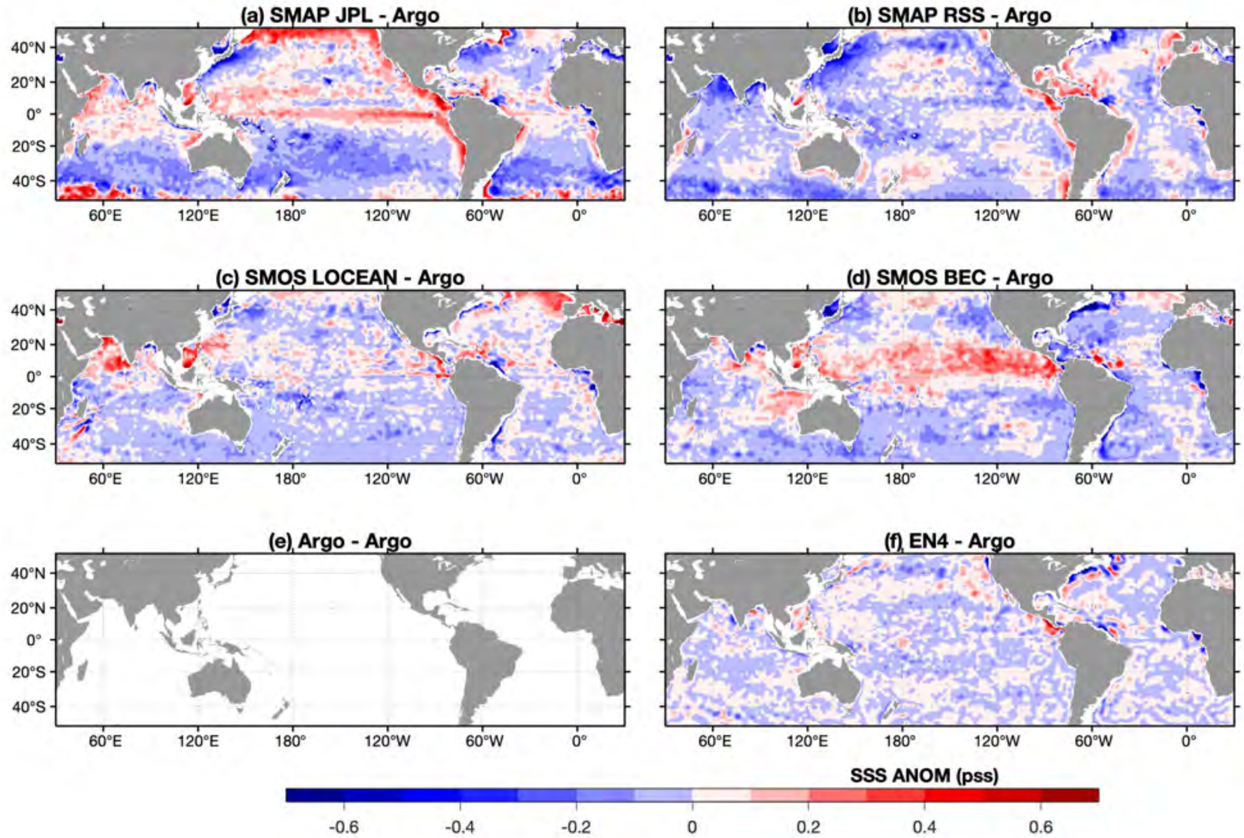

Figure 3. Difference anomaly fields referenced to the Argo mean SSS. (a) SMAP JPL – Argo, (b) SMAP RSS – Argo, (c) SMOS LOCEAN – Argo, (d) SMOS BEC – Argo, (e) Argo – Argo, and (f) EN4 – Argo. In (a)-(d), the satellite products were reconstructed on Argo 1x1 grids.

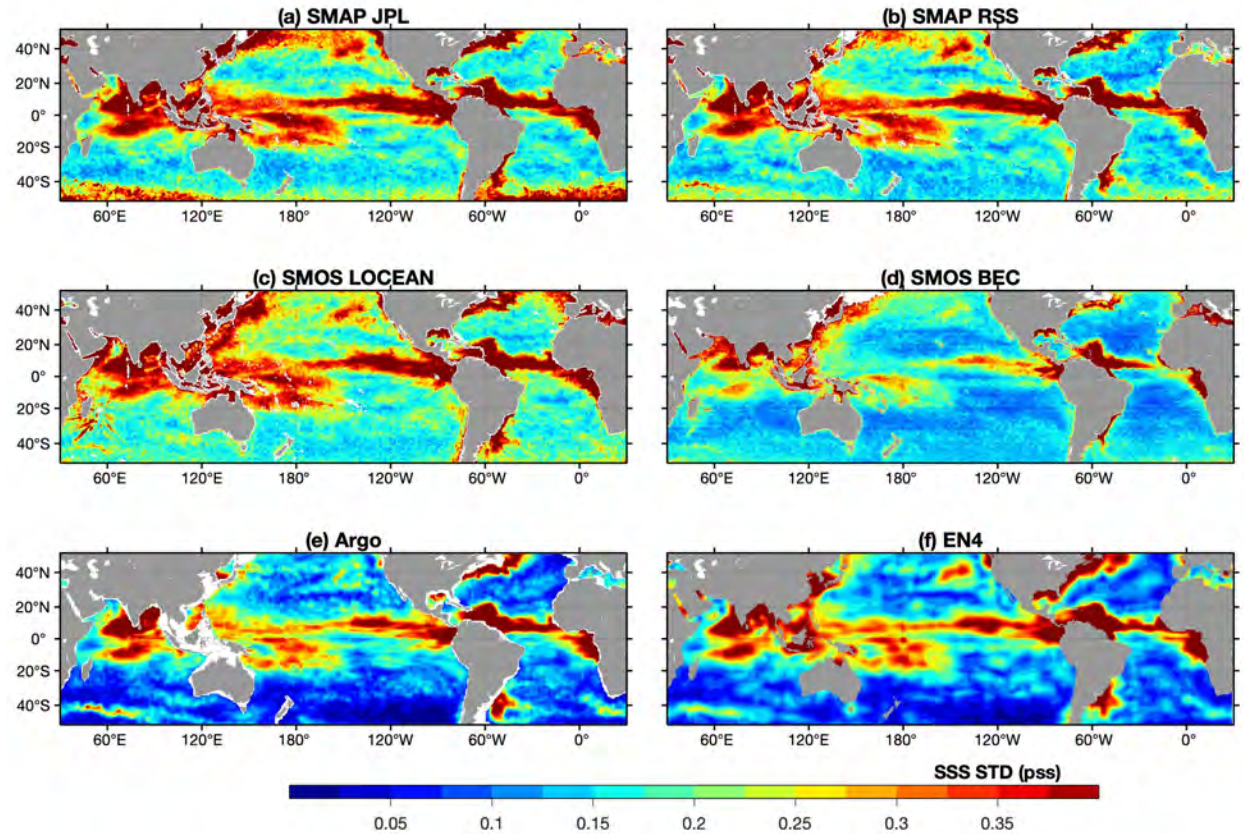

Figure 4. Standard deviation of monthly-mean SSS based on (a) SMAP JPL, (b) SMAP RSS, (c) SMOS LOCEAN, (d) SMOS BEC, (e) Argo, and (f) EN4.

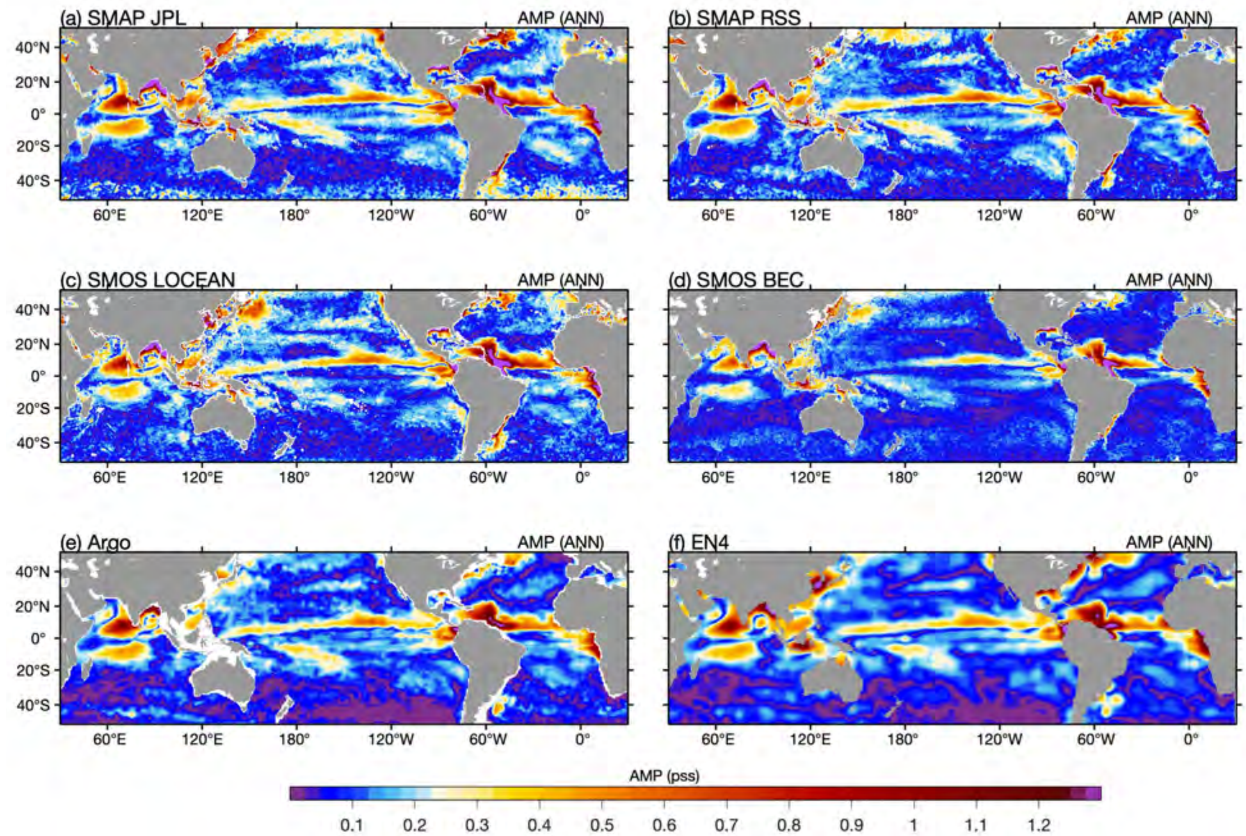

Figure 5. Amplitude of the estimated annual harmonic for (a) SMAP JPL, (b) SMAP RSS, (c) SMOS LOCEAN, (d) SMOS BEC, (e) Argo, and (f) EN4.

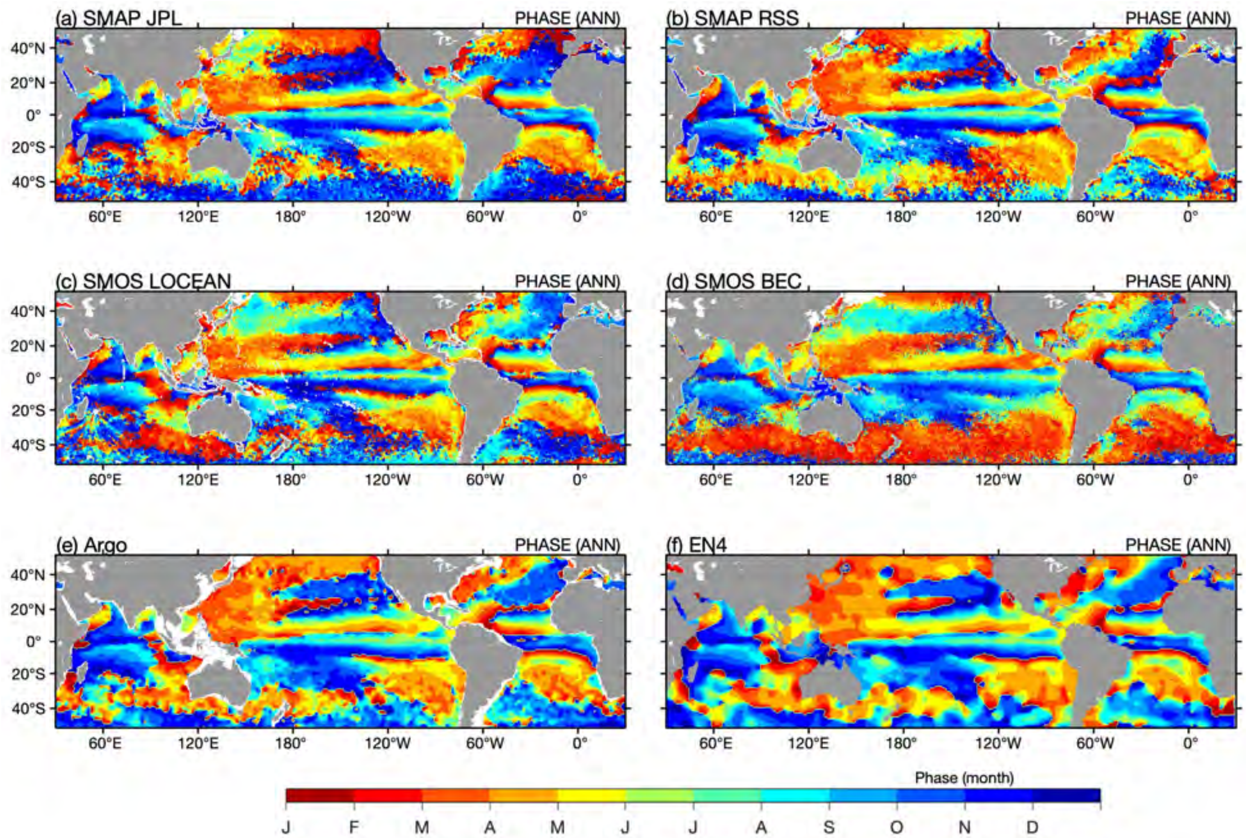

Figure 6. Phase of the estimated annual harmonic for (a) SMAP JPL, (b) SMAP RSS, (c) SMOS LOCEAN, (d) SMOS BEC, (e) Argo, and (f) EN4.

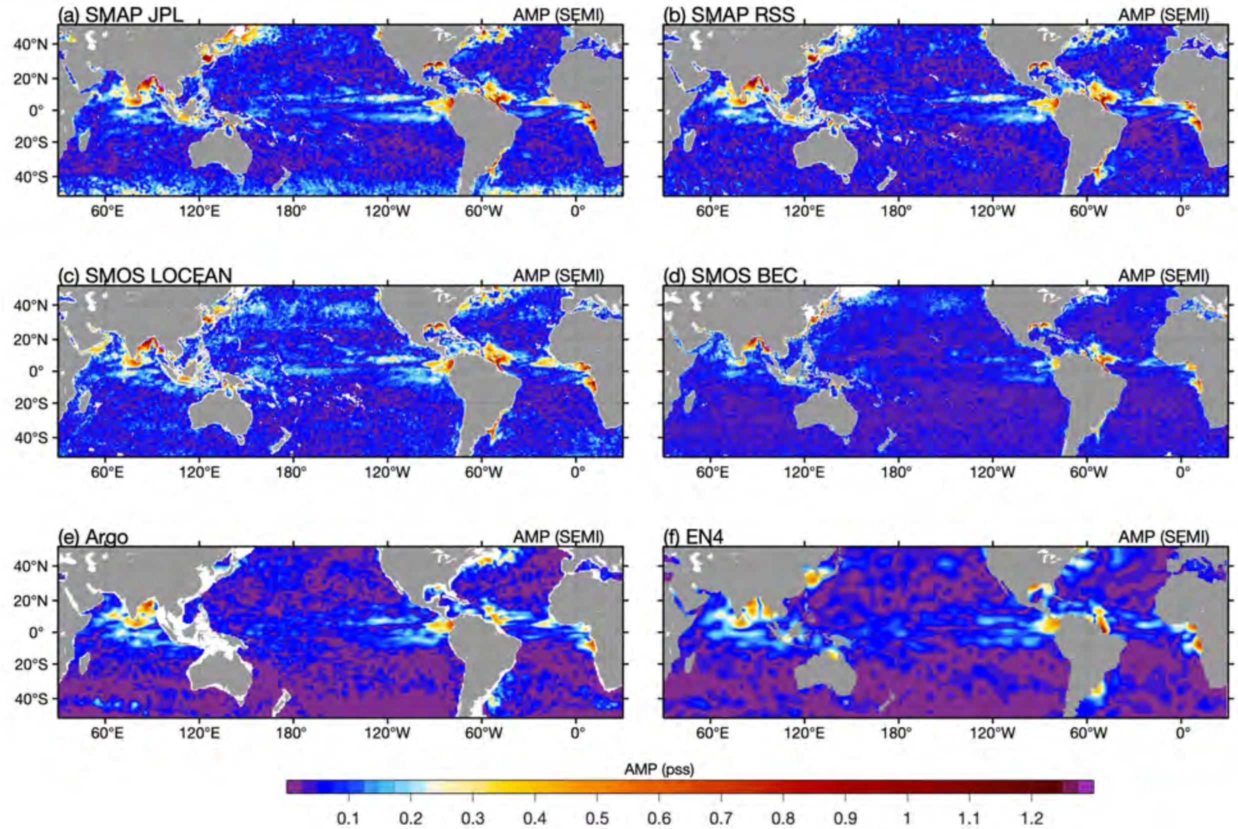

Figure 7. Same as Figure 5 but for the estimated semiannual harmonic

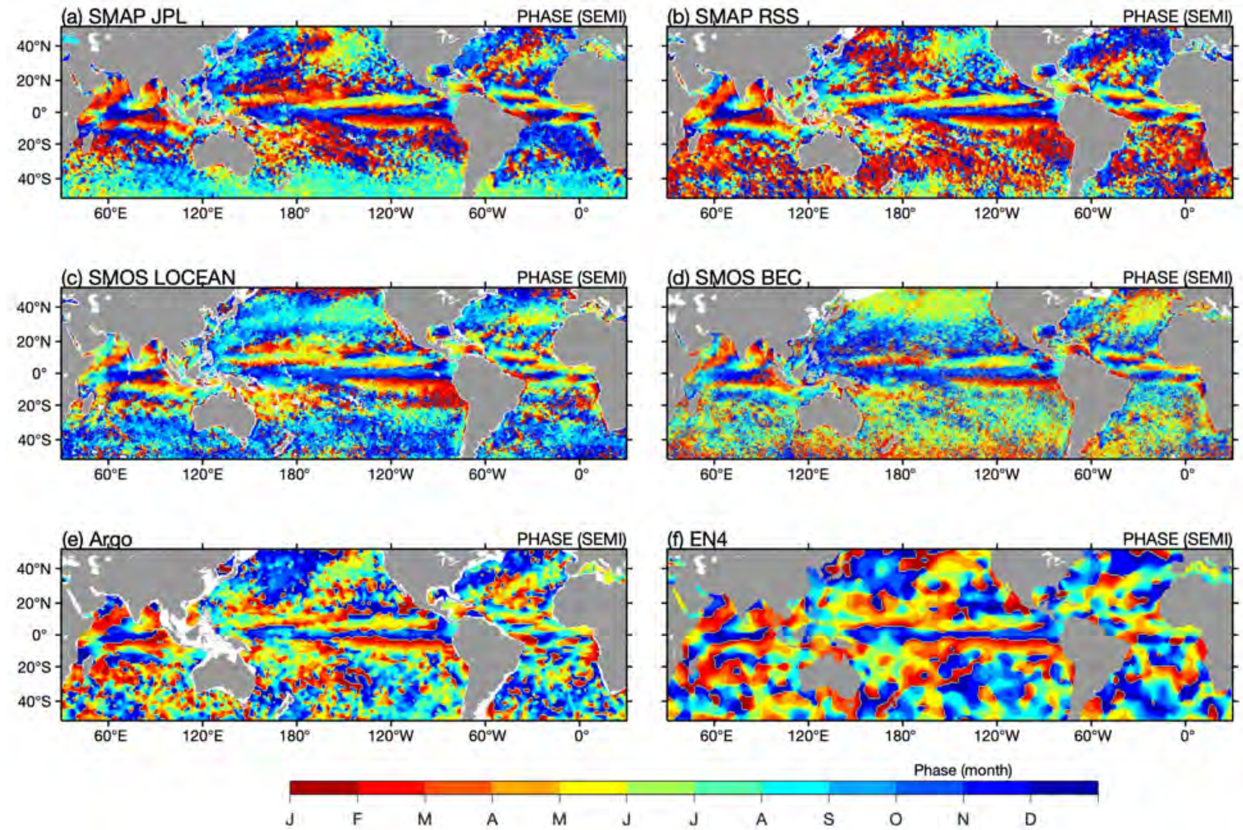

Figure 8. Same as Figure 6 but for the estimated semiannual harmonic.

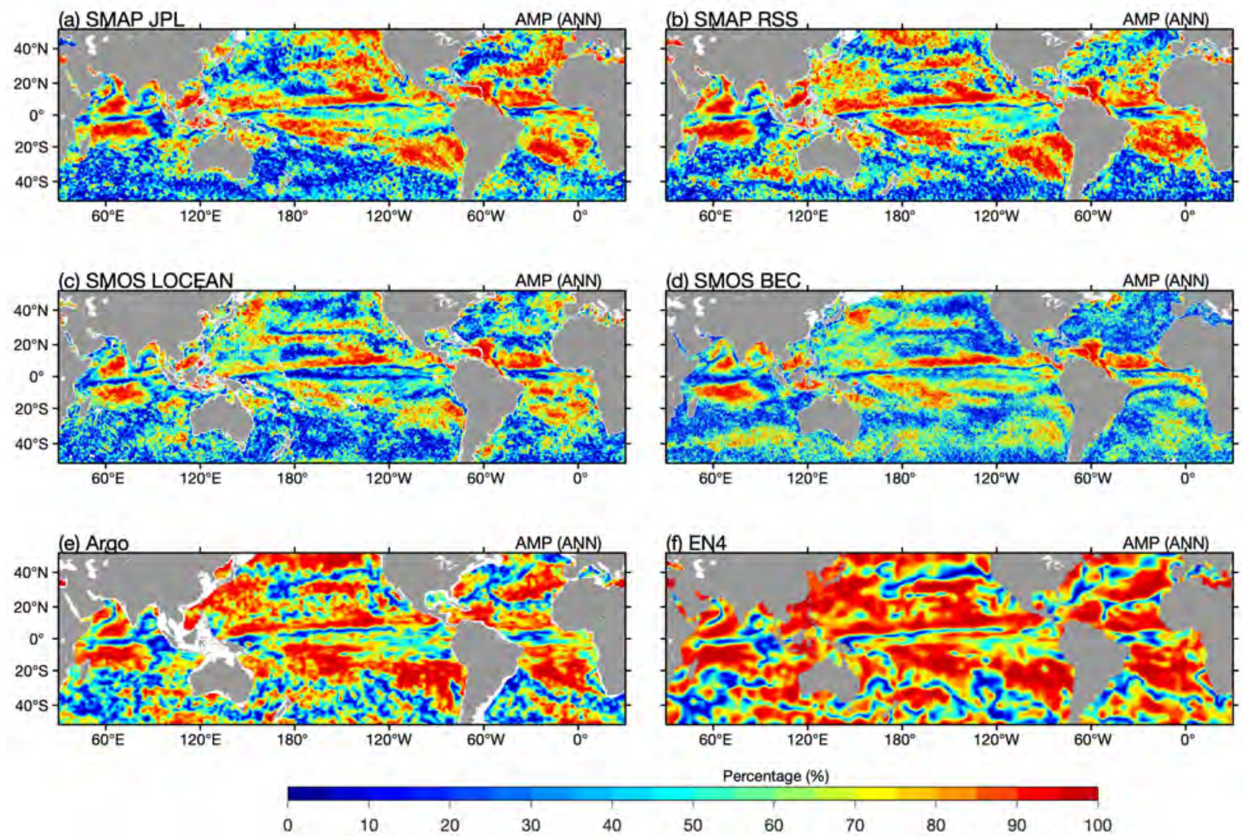

Figure 9. Percentage of total variance that can be explained by annual harmonic

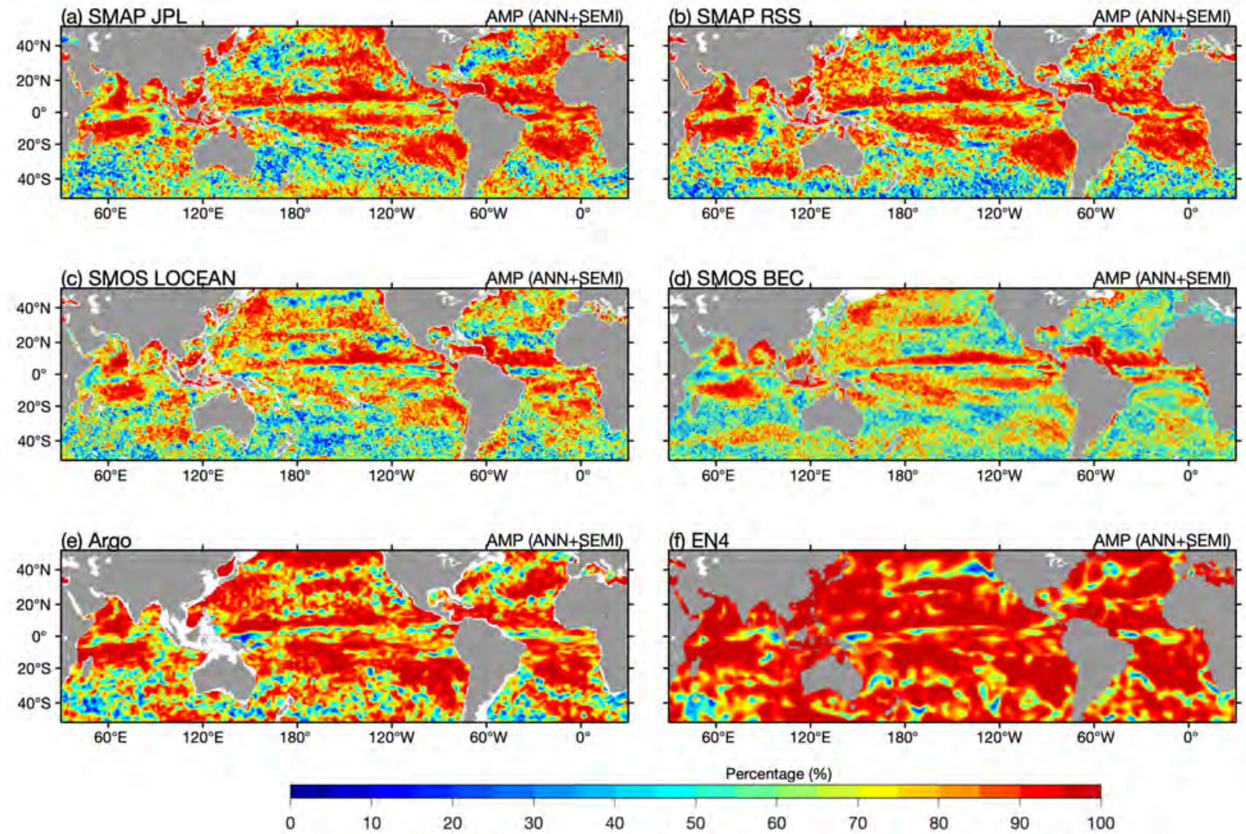

Figure 10. Same as Figure 9 but for the reconstructed seasonal cycle.

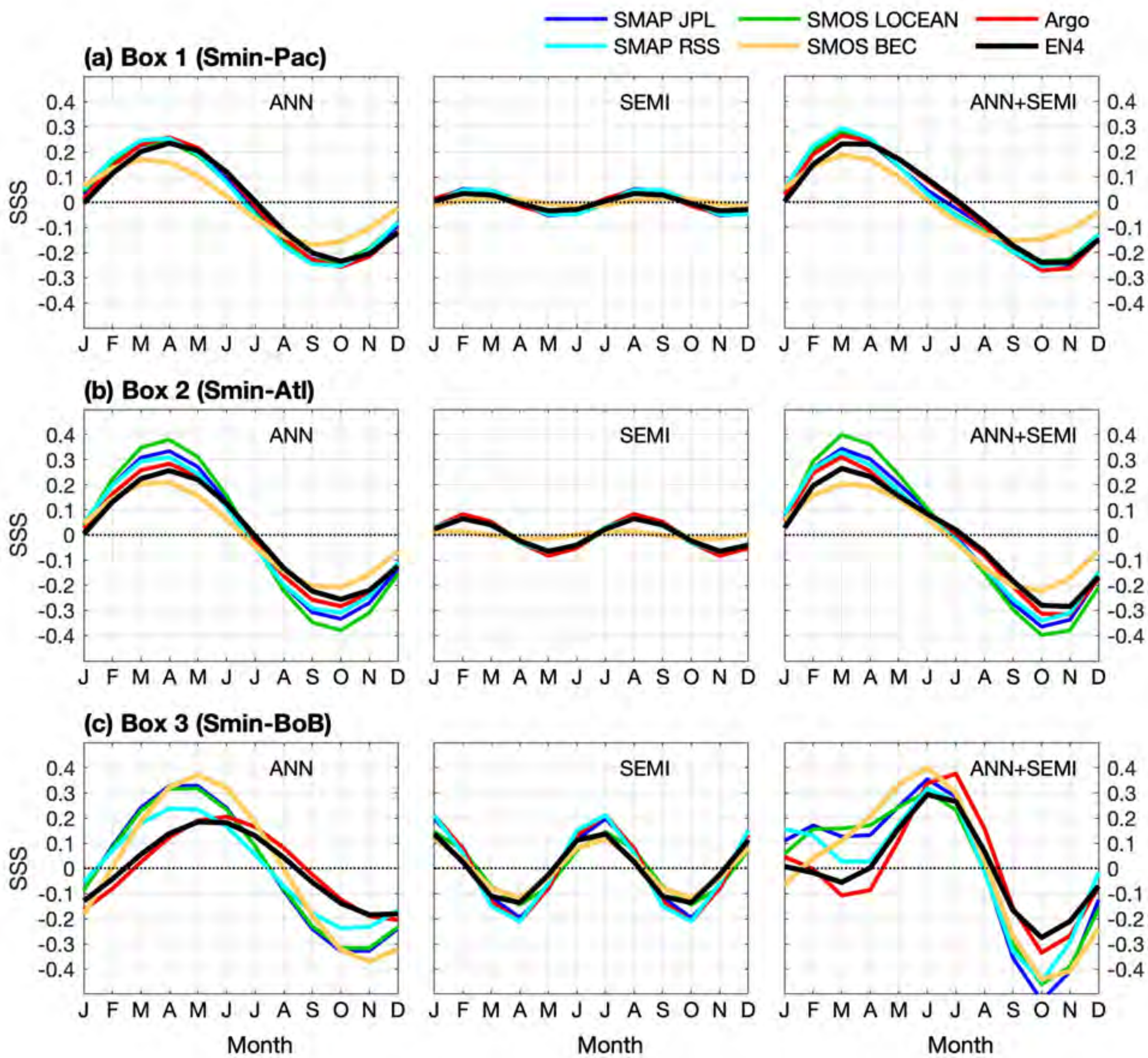

Figure 11. (left) annual cycle, (center) semiannual cycle, and (right) reconstructed seasonal variations (combined annual and semiannual modes) averaged over (a) Box 1 (Smin-Pac), (b) Box 2 (Smin-Atl), and (c) Box 3 (Smin-BoB).

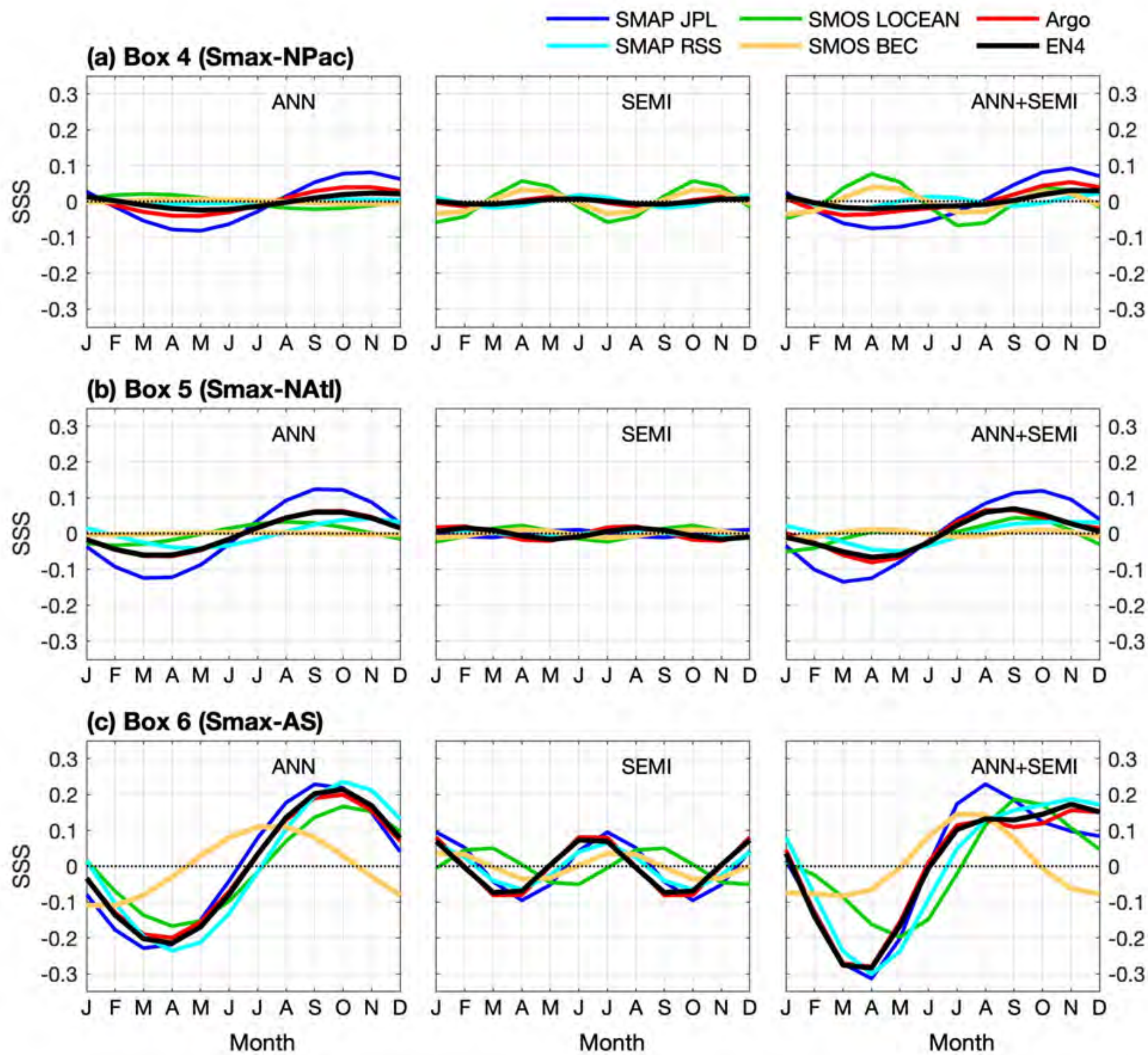

Figure 12. Same as Figure 11 but for (a) Box 4 (Smax-NPac), (b) Box 5 (Smax – NAtl), and (c) Box 6 (Smax – AS).

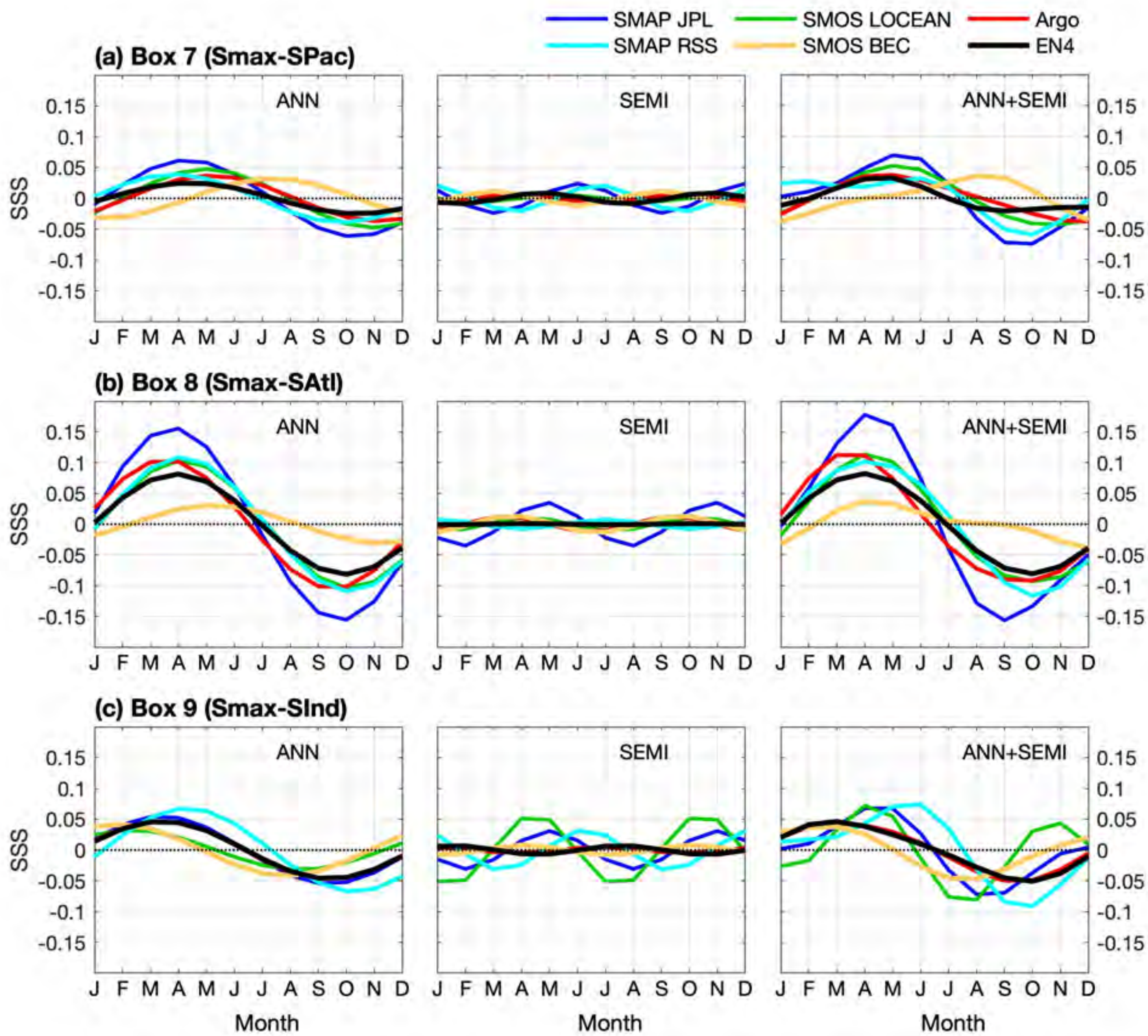

Figure 13. Same as Figure 11 but for (a) Box 7 (Smax-SPac), (b) Box 8 (Smax – SAtl), and (c) Box 9 (Smax – SInd).

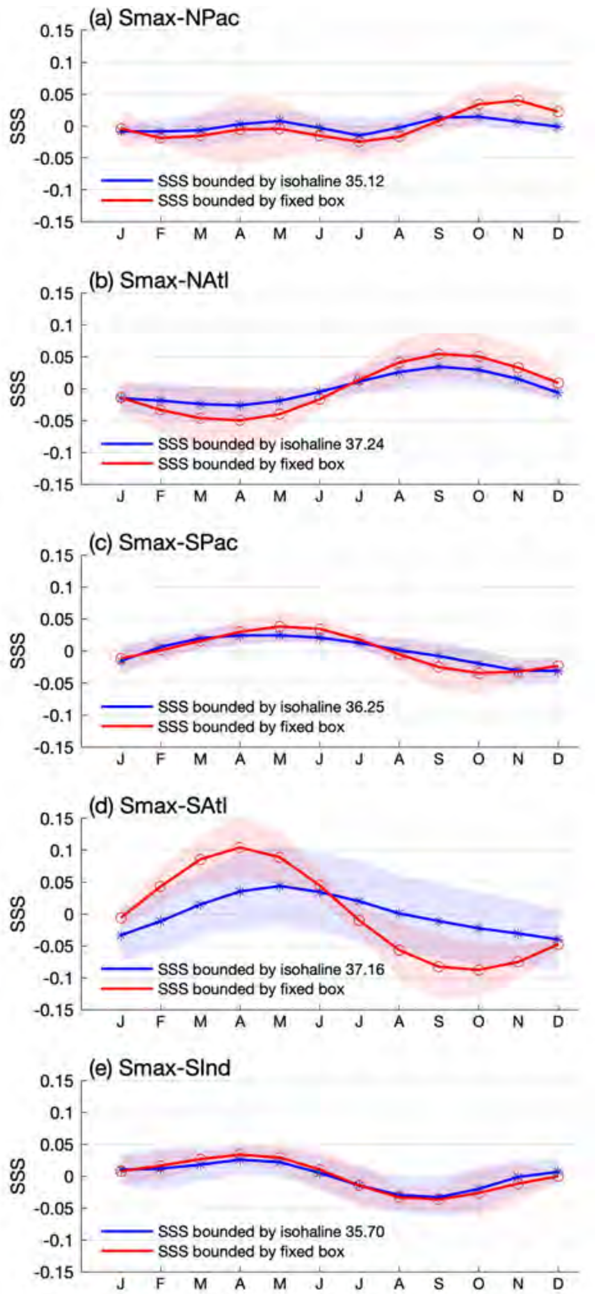

Figure 14. The seasonal cycle of the reconstructed time series averaged over five subtropical salinity maximum centers bounded by a fixed box (red line) and by the selected isohaline (blue line). The lighter color shading denotes one standard deviation between six products.

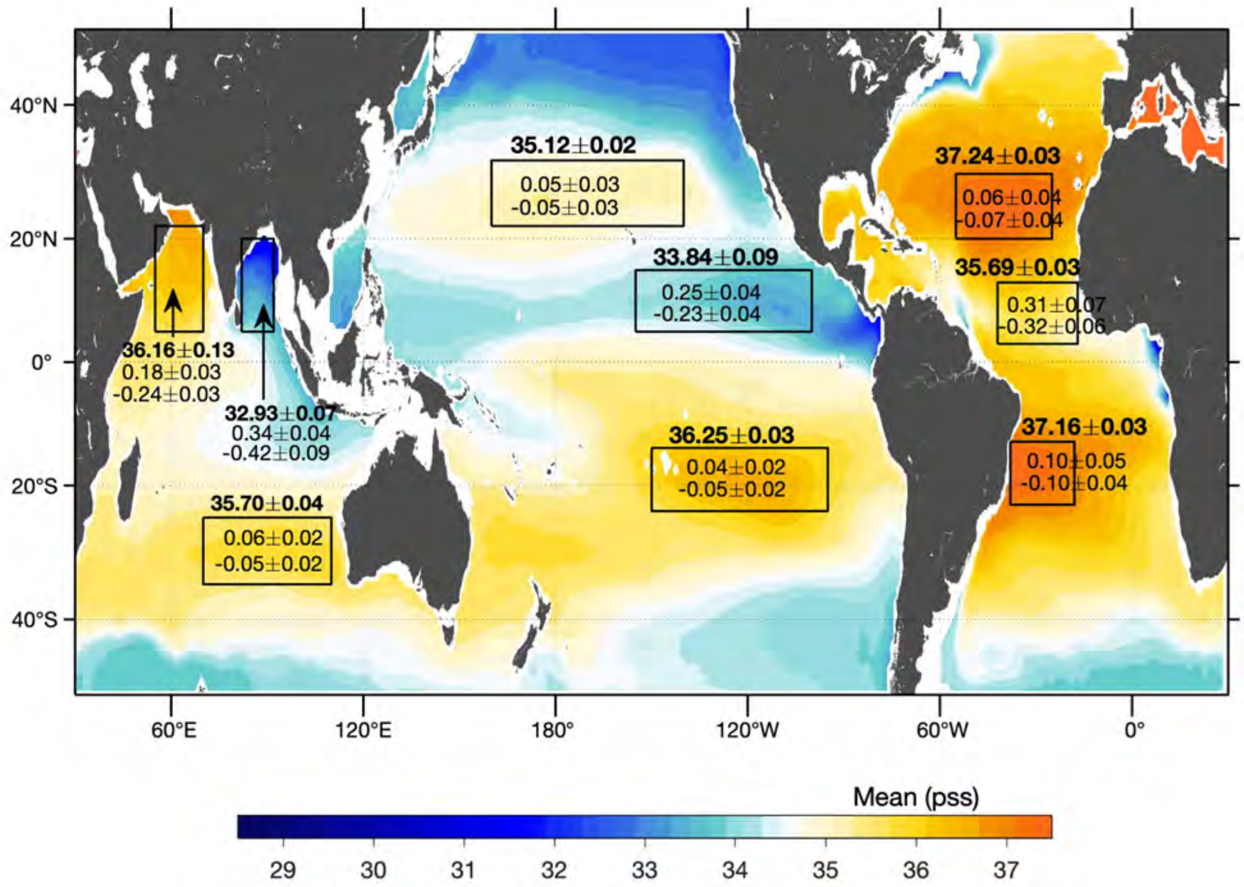

Figure 15. Summary of the mean and standard error (bold-face numbers) as well as the seasonal ranges (light-face numbers) for each boxed region. The mean and standard error were computed as the product ensemble mean and spread (STD) (see Table 2). The seasonal ranges were based on the maximum and minimum estimated from the reconstructed time series averaged over the nine selected boxes (see Table 5).